Measurement of *CP* violation and the B_s^0 meson decay width difference with $B_s^0 \rightarrow J/\psi K^+ K^-$ and $B_s^0 \rightarrow J/\psi \pi^+ \pi^-$ decays

R. Aaij *et al.**

(LHCb Collaboration)

The time-dependent *CP* asymmetry in $B_s^0 \rightarrow J/\psi K^+ K^-$ decays is measured using pp collision data at $\sqrt{s} = 7$ TeV, corresponding to an integrated luminosity of 1.0 fb^{-1}, collected with the LHCb detector. The decay-time distribution is characterized by the decay widths Γ_L and Γ_H of the light and heavy mass eigenstates of the B_s^0-$\bar{B}_s^0$ system and by a *CP*-violating phase ϕ_s. In a sample of 27 617 $B_s^0 \rightarrow J/\psi K^+ K^-$ decays, where the dominant contribution comes from $B_s^0 \rightarrow J/\psi \phi$ decays, these parameters are measured to be $\phi_s = 0.07 \pm 0.09(\text{stat}) \pm 0.01(\text{syst})$ rad, $\Gamma_s \equiv (\Gamma_L + \Gamma_H)/2 = 0.663 \pm 0.005(\text{stat}) \pm 0.006(\text{syst})$ ps^{-1}, and $\Delta\Gamma_s \equiv \Gamma_L - \Gamma_H = 0.100 \pm 0.016(\text{stat}) \pm 0.003(\text{syst})$ ps^{-1}, corresponding to the single most precise determination of ϕ_s, $\Delta\Gamma_s$, and Γ_s. The result of performing a combined analysis with $B_s^0 \rightarrow J/\psi \pi^+ \pi^-$ decays gives $\phi_s = 0.01 \pm 0.07(\text{stat}) \pm 0.01(\text{syst})$ rad, $\Gamma_s = 0.661 \pm 0.004(\text{stat}) \pm 0.006(\text{syst})$ ps^{-1}, and $\Delta\Gamma_s = 0.106 \pm 0.011(\text{stat}) \pm 0.007(\text{syst})$ ps^{-1}. All measurements are in agreement with the Standard Model predictions.

I. INTRODUCTION

The interference between B_s^0 meson decay amplitudes to *CP* eigenstates $J/\psi X$ directly or via mixing gives rise to a measurable *CP*-violating phase ϕ_s. In the Standard Model (SM), for $b \rightarrow c\bar{c}s$ transitions and ignoring subleading penguin contributions, this phase is predicted to be $-2\beta_s$, where $\beta_s = \arg(-V_{ts}V_{tb}^*/V_{cs}V_{cb}^*)$ and V_{ij} are elements of the Cabibbo-Kobayashi-Maskawa quark flavor mixing matrix [1]. The indirect determination via global fits to experimental data gives $2\beta_s = 0.0364 \pm 0.0016$ rad [2]. This precise indirect determination within the SM makes the measurement of ϕ_s interesting since new physics processes could modify the phase if new particles were to contribute to the B_s^0-$\bar{B}_s^0$ box diagrams [3,4] shown in Fig. 1.

Direct measurements of ϕ_s using $B_s^0 \rightarrow J/\psi \phi$ and $B_s^0 \rightarrow J/\psi \pi^+ \pi^-$ decays have been reported previously. In the $B_s^0 \rightarrow J/\psi \phi$ channel, the decay width difference of the light (L) and heavy (H) B_s^0 mass eigenstates, $\Delta\Gamma_s \equiv \Gamma_L - \Gamma_H$, and the average B_s^0-decay width, $\Gamma_s = (\Gamma_L + \Gamma_H)/2$, are also measured. The measurements of ϕ_s and $\Delta\Gamma_s$ are shown in Table I.

This paper extends previous LHCb measurements in the $B_s^0 \rightarrow J/\psi \phi$ [5] and $B_s^0 \rightarrow J/\psi \pi^+ \pi^-$ [6] channels. In the previous analysis of $B_s^0 \rightarrow J/\psi \phi$ decays, the invariant mass of the K^+K^- system was limited to ± 12 MeV/c^2 around the $\phi(1020)$ mass [11], which selected predominately resonant P-wave $\phi \rightarrow K^+K^-$ events, although a

---

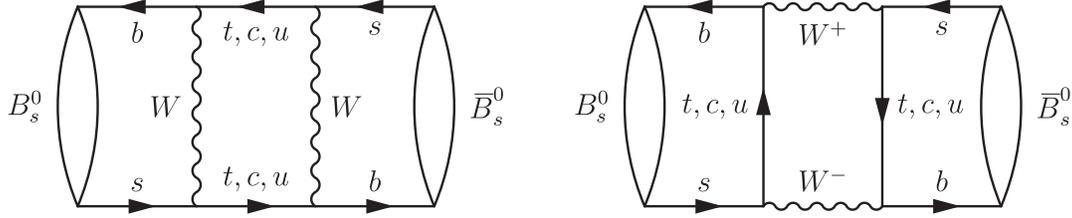*Full author list given at end of the article.

small S-wave K^+K^- component was also present. In this analysis the K^+K^- mass range is extended to ± 30 MeV/c^2, and the notation $B_s^0 \rightarrow J/\psi K^+ K^-$ is used to include explicitly both P- and S-wave decays [12]. In both channels additional same-side flavor-tagging information is used. The data were obtained from pp collisions collected by the LHCb experiment at a center-of-mass energy of 7 TeV during 2011, corresponding to an integrated luminosity of 1.0 fb^{-1}.

This paper is organized as follows. Section II presents the phenomenological aspects related to the measurement. Section III presents the LHCb detector. In Sec. IV the selection of $B_s^0 \rightarrow J/\psi K^+ K^-$ candidates is described. Section V deals with decay-time resolution, Sec. VI deals with the decay-time and angular acceptance effects, and Sec. VII deals with flavor tagging. The maximum likelihood fit is explained in Sec. VIII. The results and systematic uncertainties for the $B_s^0 \rightarrow J/\psi K^+ K^-$ channel are given in Secs. IX and X, the results for the $B_s^0 \rightarrow J/\psi \pi^+ \pi^-$ channel are given in Sec. XI, and finally the combined results are presented in Sec. XII. Charge conjugation is implied throughout the paper.

II. PHENOMENOLOGY

The $B_s^0 \rightarrow J/\psi K^+ K^-$ decay proceeds predominantly via $B_s^0 \rightarrow J/\psi \phi$ with the ϕ meson subsequently decaying to K^+K^-. In this case there are two intermediate vector particles, and the K^+K^- pair is in a P-wave configuration. The final state is then a superposition of *CP*-even and *CP*-odd states depending upon the relative orbital angular momentum of the J/ψ and the ϕ. The phenomenological aspects of this process are described in many articles, e.g., Refs. [13,14]. The main Feynman diagrams for $B_s^0 \rightarrow J/\psi K^+ K^-$ decays are shown in Fig. 2. The effects induced

FIG. 1.   Feynman diagrams for B_s^0-$\bar{B}_s^0$ mixing, within the SM.

by the subleading penguin contributions are discussed, e.g., in Ref. [15]. The same final state can also be produced with K^+K^- pairs in an S-wave configuration [16]. This S-wave final state is *CP*-odd. The measurement of ϕ_s requires the *CP*-even and *CP*-odd components to be disentangled by analyzing the distribution of the reconstructed decay angles of the final-state particles.

In contrast to Ref. [5], this analysis uses the decay angles defined in the helicity basis, as this simplifies the angular description of the background and acceptance. The helicity angles are denoted by $\Omega = (\cos\theta_K, \cos\theta_\mu, \varphi_h)$, and their definition is shown in Fig. 3. The polar angle θ_K (θ_μ) is the angle between the K^+ (μ^+) momentum and the direction opposite to the B_s^0 momentum in the K^+K^- ($\mu^+\mu^-$) center-of-mass system. The azimuthal angle between the K^+K^- and $\mu^+\mu^-$ decay planes is φ_h. This angle is defined by a rotation from the K^- side of the K^+K^- plane to the μ^+ side of the $\mu^+\mu^-$ plane. The rotation is positive in the $\mu^+\mu^-$ direction in the B_s^0 rest frame. A definition of the angles in terms of the particle momenta is given in the Appendix.

The decay can be decomposed into four time-dependent complex amplitudes, $A_i(t)$. Three of these arise in the P-wave decay and correspond to the relative orientation of the linear polarization vectors of the J/ψ and ϕ mesons, where $i \in \{0, \|, \perp\}$ and refers to the longitudinal, transverse-parallel, and transverse-perpendicular orientations, respectively. The single K^+K^- S-wave amplitude is denoted by $A_S(t)$.

The distribution of the decay time and angles for a B_s^0 meson produced at time $t = 0$ is described by a sum of ten terms, corresponding to the four polarization amplitudes

and their interference terms. Each of these is given by the product of a time-dependent function and an angular function [13]:

$$\frac{\mathrm{d}^4\Gamma(B_s^0 \to J/\psi K^+K^-)}{\mathrm{d}t\mathrm{d}\Omega} \propto \sum_{k=1}^{10} h_k(t)f_k(\Omega). \quad (1)$$

The time-dependent functions $h_k(t)$ can be written as

$$h_k(t) = N_k e^{-\Gamma_s t}\left[a_k \cosh\left(\frac{1}{2}\Delta\Gamma_s t\right) + b_k \sinh\left(\frac{1}{2}\Delta\Gamma_s t\right)\right.$$
$$\left. + c_k \cos\left(\Delta m_s t\right) + d_k \sin\left(\Delta m_s t\right)\right], \quad (2)$$

where Δm_s is the mass difference between the heavy and light B_s^0 mass eigenstates. The expressions for the $f_k(\Omega)$ and the coefficients of Eq. 2 are given in Table II [17,18]. The coefficients N_k are expressed in terms of the $A_i(t)$ at $t = 0$, from now on denoted as A_i. The amplitudes are parametrized by $|A_i|e^{i\delta_i}$ with the conventions $\delta_0 = 0$ and $|A_0|^2 + |A_\||^2 + |A_\perp|^2 = 1$. The S-wave fraction is defined as $F_S = |A_S|^2/(|A_0|^2 + |A_\||^2 + |A_\perp|^2 + |A_S|^2) = |A_S|^2/(|A_S|^2 + 1)$.

For the coefficients $a_k, \ldots, d_k$, three *CP*-violating observables are introduced;

$$C \equiv \frac{1 - |\lambda|^2}{1 + |\lambda|^2}, \qquad S \equiv \frac{2\Im(\lambda)}{1 + |\lambda|^2}, \qquad D \equiv -\frac{2\Re(\lambda)}{1 + |\lambda|^2}, \quad (3)$$

where the parameter λ is defined below. These definitions for S and C correspond to those adopted by HFAG [19], and the sign of D is chosen such that it is equivalent to the symbol $A_f^{\Delta\Gamma}$ used in Ref. [19]. The *CP*-violating phase ϕ_s

TABLE I.   Results for ϕ_s and $\Delta\Gamma_s$ from different experiments. The first uncertainty is statistical, and the second is systematic (apart from the D0 result, for which the uncertainties are combined). The CDF confidence level (C.L.) range quoted is that consistent with other experimental measurements of ϕ_s.

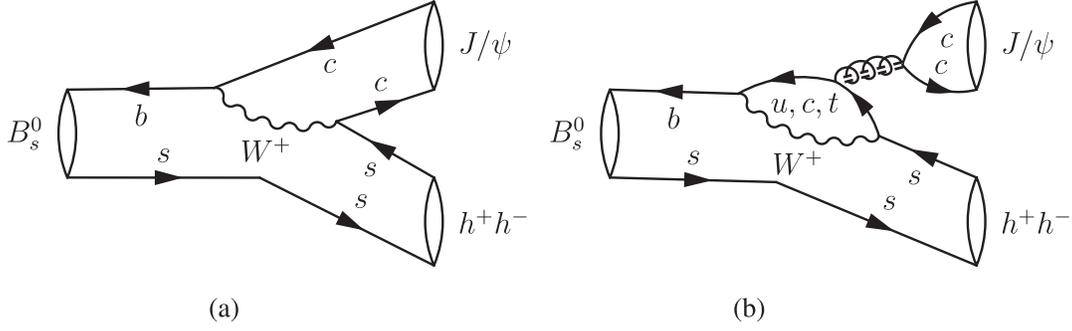| Experiment	Data set [fb^{-1}]	References	ϕ_s [rad]	$\Delta\Gamma_s$ [ps^{-1}]
LHCb ($B_s^0 \to J/\psi\phi$)	0.4	[5]	$0.15 \pm 0.18 \pm 0.06$	$0.123 \pm 0.029 \pm 0.011$
LHCb ($B_s^0 \to J/\psi\pi^+\pi^-$)	1.0	[6]	$-0.019^{+0.173+0.004}_{-0.174-0.003}$	$\cdots$
LHCb (combined)	0.4 + 1.0	[6]	$0.06 \pm 0.12 \pm 0.06$	$\cdots$
ATLAS	4.9	[7]	$0.22 \pm 0.41 \pm 0.10$	$0.053 \pm 0.021 \pm 0.010$
CMS	5.0	[8]	$\cdots$	$0.048 \pm 0.024 \pm 0.003$
D0	8.0	[9]	$-0.55^{+0.38}_{-0.36}$	$0.163^{+0.065}_{-0.064}$
CDF	9.6	[10]	$[-0.60, 0.12]$ at 68% C.L.	$0.068 \pm 0.026 \pm 0.009$

FIG. 2.   Feynman diagrams contributing to the decay $B_s^0 \rightarrow J/\psi h^+ h^-$ within the SM, where $h = \pi, K$. (a) Tree; (b) Penguin.
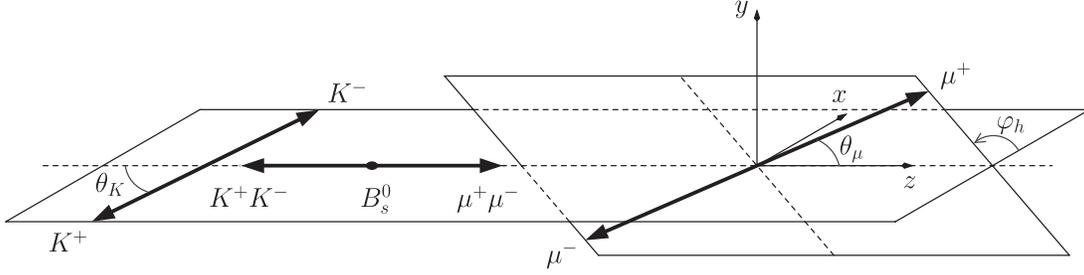
FIG. 3.   Definition of helicity angles as discussed in the text.

is defined by $\phi_s \equiv -\arg(\lambda)$, and hence S and D can be written as

$$S \equiv -\frac{2|\lambda|\sin\phi_s}{1+|\lambda|^2}, \qquad D \equiv -\frac{2|\lambda|\cos\phi_s}{1+|\lambda|^2}. \qquad (4)$$

The parameter λ describes *CP* violation in the interference between mixing and decay and is derived from the *CP*-violating parameter [20] associated with each polarization state i,

$$\lambda_i \equiv \frac{q}{p}\frac{\bar{A}_i}{A_i}, \qquad (5)$$

where A_i $(\bar{A}_i)$ is the amplitude for a B_s^0 $(\bar{B}_s^0)$ meson to decay to final state i and the complex parameters $p = \langle B_s^0|B_L\rangle$ and $q = \langle\bar{B}_s^0|B_L\rangle$ describe the relation between mass and flavor eigenstates. The polarization states i have the *CP*

eigenvalue $\eta_i = +1$ for $i \in \{0, \|\}$, and $\eta_i = -1$ for $i \in \{\perp, S\}$. Assuming that any possible *CP* violation in the decay is the same for all amplitudes, then the product $\eta_i\bar{A}_i/A_i$ is independent of i. The polarization-independent *CP*-violating parameter λ is then defined such that $\lambda_i = \eta_i\lambda$. The differential decay rate for a $\bar{B}_s^0$ meson produced at time $t = 0$ can be obtained by changing the sign of c_k and d_k and by including a relative factor $|p/q|^2$.

The expressions are invariant under the transformation

$$(\phi_s, \Delta\Gamma_s, \delta_0, \delta_\|, \delta_\perp, \delta_S)$$
$$\mapsto (\pi - \phi_s, -\Delta\Gamma_s, -\delta_0, -\delta_\|, \pi - \delta_\perp, -\delta_S), \quad (6)$$

which gives rise to a two-fold ambiguity in the results.

TABLE II.   Definition of angular and time-dependent functions.

k	$f_k(\theta_\mu, \theta_K, \varphi_h)$	N_k	a_k	b_k	c_k	d_k
1	$2\cos^2\theta_K\sin^2\theta_\mu$	$|A_0|^2$	1	D	C	$-S$
2	$\sin^2\theta_K(1-\sin^2\theta_\mu\cos^2\varphi_h)$	$|A_\||^2$	1	D	C	$-S$
3	$\sin^2\theta_K(1-\sin^2\theta_\mu\sin^2\varphi_h)$	$|A_\perp|^2$	1	$-D$	C	S
4	$\sin^2\theta_K\sin^2\theta_\mu\sin 2\varphi_h$	$|A_\|A_\perp|$	$C\sin(\delta_\perp-\delta_\|)$	$S\cos(\delta_\perp-\delta_\|)$	$\sin(\delta_\perp-\delta_\|)$	$D\cos(\delta_\perp-\delta_\|)$
5	$\frac{1}{2}\sqrt{2}\sin 2\theta_K\sin 2\theta_\mu\cos\varphi_h$	$|A_0A_\||$	$\cos(\delta_\|-\delta_0)$	$D\cos(\delta_\|-\delta_0)$	$C\cos(\delta_\|-\delta_0)$	$-S\cos(\delta_\|-\delta_0)$
6	$-\frac{1}{2}\sqrt{2}\sin 2\theta_K\sin 2\theta_\mu\sin\varphi_h$	$|A_0A_\perp|$	$C\sin(\delta_\perp-\delta_0)$	$S\cos(\delta_\perp-\delta_0)$	$\sin(\delta_\perp-\delta_0)$	$D\cos(\delta_\perp-\delta_0)$
7	$\frac{2}{3}\sin^2\theta_\mu$	$|A_S|^2$	1	$-D$	C	S
8	$\frac{1}{3}\sqrt{6}\sin\theta_K\sin 2\theta_\mu\cos\varphi_h$	$|A_SA_\||$	$C\cos(\delta_\|-\delta_S)$	$S\sin(\delta_\|-\delta_S)$	$\cos(\delta_\|-\delta_S)$	$D\sin(\delta_\|-\delta_S)$
9	$-\frac{1}{3}\sqrt{6}\sin\theta_K\sin 2\theta_\mu\sin\varphi_h$	$|A_SA_\perp|$	$\sin(\delta_\perp-\delta_S)$	$-D\sin(\delta_\perp-\delta_S)$	$C\sin(\delta_\perp-\delta_S)$	$S\sin(\delta_\perp-\delta_S)$
10	$\frac{4}{3}\sqrt{3}\cos\theta_K\sin^2\theta_\mu$	$|A_SA_0|$	$C\cos(\delta_0-\delta_S)$	$S\sin(\delta_0-\delta_S)$	$\cos(\delta_0-\delta_S)$	$D\sin(\delta_0-\delta_S)$

In the selected $\pi^+ \pi^-$ invariant mass range, the *CP*-odd fraction of $B_s^0 \to J/\psi \pi^+ \pi^-$ decays is greater than 97.7% at 95% C.L. as described in Ref. [21]. As a consequence, no angular analysis of the decay products is required, and the differential decay rate can be simplified to

$$\frac{\mathrm{d}\Gamma(B_s^0 \to J/\psi \pi^+ \pi^-)}{\mathrm{d}t} \propto h_7(t). \tag{7}$$

III. DETECTOR

The LHCb detector [22] is a single-arm forward spectrometer covering the pseudorapidity range $2 < \eta < 5$, designed for the study of particles containing b or c quarks. The detector includes a high-precision tracking system consisting of a silicon-strip vertex detector surrounding the pp interaction region, a large-area silicon-strip detector located upstream of a dipole magnet with a bending power of about 4 Tm, and three stations of silicon-strip detectors and straw drift tubes placed downstream. The combined tracking system has momentum resolution $\Delta p/p$ that varies from 0.4% at 5 GeV/c to 0.6% at 100 GeV/c and an impact parameter resolution of 20 μm for tracks with high transverse momentum. Charged hadrons are identified using two ring-imaging Cherenkov detectors [23]. Photon, electron, and hadron candidates are identified by a calorimeter system consisting of scintillating-pad and preshower detectors, an electromagnetic calorimeter, and a hadronic calorimeter. Muons are identified by a system composed of alternating layers of iron and multiwire proportional chambers. The trigger consists of a hardware stage, based on information from the calorimeter and muon systems, followed by a software stage that applies a full event reconstruction [24].

Simulated pp collisions are generated using PYTHIA 6.4 [25] with a specific LHCb configuration [26]. Decays of hadronic particles are described by EVTGEN [27], in which final-state radiation is generated using PHOTOS [28]. The interaction of the generated particles with the detector and its response are implemented using the GEANT4 toolkit [29] as described in Ref. [30].

IV. SELECTION OF $B_s^0 \to J/\psi K^+ K^-$ CANDIDATES

The reconstruction of $B_s^0 \to J/\psi K^+ K^-$ candidates proceeds using the decays $J/\psi \to \mu^+ \mu^-$ combined with a pair of oppositely-charged kaons. Events are first required to pass a hardware trigger [24], which selects events containing muon or hadron candidates with a high transverse momentum (p_{T}). The subsequent software trigger [24] is composed of two stages, the first of which performs a partial event reconstruction. Two types of first-stage software triggers are employed. For the first type, events are required to have two well-identified oppositely-charged muons with invariant mass larger than 2.7 GeV/c^2. This trigger has an almost uniform acceptance as a function of

decay time and will be referred to as unbiased. For the second type, there must be at least one muon (one high-p_{T} track) with a transverse momentum larger than 1 GeV/c (1.7 GeV/c) and an impact parameter larger than 100 μm with respect to the primary vertex (PV). This trigger introduces a nontrivial acceptance as a function of decay time and will be referred to as biased. The second stage of the trigger performs a full event reconstruction and only retains events containing a $\mu^+ \mu^-$ pair with invariant mass within 120 MeV/c^2 of the J/ψ mass [11] and that form a vertex that is significantly displaced from the PV, introducing another small decay-time biasing effect.

The final B_s^0 candidate selection is performed by applying kinematic and particle identification criteria to the final-state tracks. The J/ψ meson candidates are formed from two oppositely-charged particles, originating from a common vertex, which have been identified as muons and which have p_{T} larger than 500 MeV/c. The invariant mass of the $\mu^+ \mu^-$ pair, $m(\mu^+ \mu^-)$, must be in the range [3030, 3150] MeV/c^2. During subsequent steps of the selection, $m(\mu^+ \mu^-)$ is constrained to the J/ψ mass [11].

The $K^+ K^-$ candidates are formed from two oppositely-charged particles that have been identified as kaons and that originate from a common vertex. The $K^+ K^-$ pair is required to have a p_{T} larger than 1 GeV/c. The invariant mass of the $K^+ K^-$ pair, $m(K^+ K^-)$, must be in the range [990, 1050] MeV/c^2.

The B_s^0 candidates are reconstructed by combining the J/ψ candidate with the $K^+ K^-$ pair, requiring their invariant mass $m(J/\psi K^+ K^-)$ to be in the range [5200, 5550] MeV/c^2. The decay time, t, of the B_s^0 candidate is calculated from a vertex and kinematic fit that constrains the $B_s^0 \to J/\psi K^+ K^-$ candidate to originate from its associated PV [31]. The χ^2 of the fit (which has 7 degrees of freedom) is required to be less than 35. Multiple B_s^0 candidates are found in less than 1% of events; in these cases the candidate with the smallest χ^2 is chosen. B_s^0 candidates are required to have decay time in the range [0.3, 14.0] ps; the lower bound on the decay time suppresses a large fraction of the prompt combinatorial background while having a negligible effect on the sensitivity to ϕ_s. The kinematic fit evaluates an estimated decay-time uncertainty, σ_t. Candidates with σ_t larger than 0.12 ps are removed from the event sample.

Figure 4 shows the $m(J/\psi K^+ K^-)$ distribution for events originating from both the unbiased and biased triggers, along with corresponding projection of an unbinned maximum log-likelihood fit to the sample. The probability density function (PDF) used for the fit is composed of the sum of two Gaussian functions with a common mean and separate widths and an exponential function for the combinatorial background. In total, after the trigger and full offline selection requirements, there are $27\,617 \pm 115$ $B_s^0 \to J/\psi K^+ K^-$ signal events found by the fit. Of these, $23\,502 \pm 107$ were selected by the unbiased trigger, and
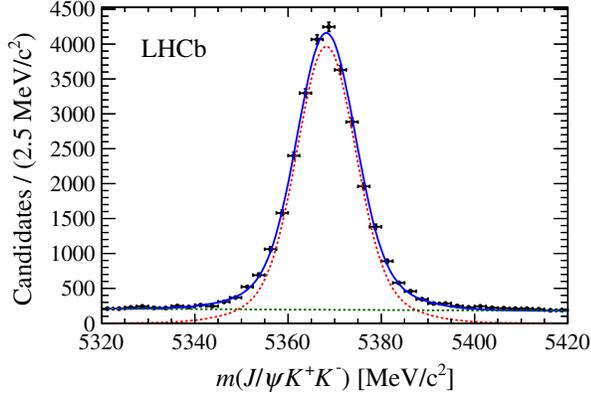
FIG. 4 (color online). Invariant-mass distribution of the selected $B_s^0 \rightarrow J/\psi K^+ K^-$ candidates. The mass of the $\mu^+ \mu^-$ pair is constrained to the J/ψ mass [11]. Curves for the fitted contributions from signal (dotted red), background (dotted green), and their combination (solid blue) are overlaid.

4115 ± 43 were exclusively selected by the biased trigger. The uncertainties quoted here come from propagating the uncertainty on the signal fraction evaluated by the fit.

Figure 5 shows the invariant mass of the $\mu^+ \mu^-$ and $K^+ K^-$ pairs satisfying the selection requirements. The background has been subtracted using the *sPlot* [32] technique with $m(J/\psi K^+ K^-)$ as the discriminating variable. In both cases fits are also shown. For the dimuon system, the fit model is a double Crystal-Ball shape [33]. For the dikaon system, the total fit model is the sum of a relativistic P-wave Breit-Wigner distribution convolved with a Gaussian function to model the dominant ϕ-meson peak and a polynomial function to describe the small $K^+ K^-$ S-wave component.

V. DECAY-TIME RESOLUTION

If the decay-time resolution is not negligibly small compared to the B_s^0-meson oscillation period $2\pi/\Delta m_s \approx 350$ fs, it affects the measurement of the oscillation amplitude, and thereby ϕ_s. For a given decay-time resolution,

σ_t, the dilution of the amplitude can be expressed as $\mathcal{D} = \exp(-\sigma_t^2 \Delta m_s^2/2)$ [34]. The relative systematic uncertainty on the dilution directly translates into a relative systematic uncertainty on ϕ_s.

For each reconstructed candidate, σ_t is estimated by the vertex fit with which the decay time is calculated. The signal distribution of σ_t is shown in Fig. 6, where the *sPlot* technique is used to subtract the background. To account for the fact that track parameter resolutions are not perfectly calibrated and that the resolution function is not Gaussian, a triple Gaussian resolution model is constructed:

$$ R(t; \sigma_t) = \sum_{i=1}^{3} \frac{f_i}{\sqrt{2\pi} r_i \sigma_t} \exp\left[-\frac{(t-d)^2}{2 r_i^2 \sigma_t^2} \right], \quad (8) $$

where d is a common small offset of a few fs, r_i are event-independent resolution scale factors, and f_i is the fraction of each Gaussian component, normalized such that $\sum f_i = 1$.

The scale factors are estimated from a sample of prompt $\mu^+ \mu^- K^+ K^-$ combinations that pass the same selection criteria as the signal except for those that affect the decay-time distribution. This sample consists primarily of prompt combinations that have a true decay time of zero. Consequently, the shape of the decay-time distribution close to zero is representative of the resolution function itself.

Prompt combinations for which the muon pair originates from a real J/ψ meson have a better resolution than those with random muon pairs. Furthermore, fully simulated events confirm that the resolution evaluated using prompt $J/\psi \rightarrow \mu^+ \mu^-$ decays with two random kaons is more representative for the resolution of B_s^0 signal decays than the purely combinatorial background. Consequently, in the data only $J/\psi K^+ K^-$ events are used to estimate the resolution function. These are isolated using the *sPlot* method to subtract the $\mu^+ \mu^-$ combinatorial background.

The background-subtracted decay-time distribution for $J/\psi K^+ K^-$ candidates is shown in Fig. 7 using linear and logarithmic scales. The distribution is characterized by a prompt peak and a tail due to J/ψ mesons from B decays.
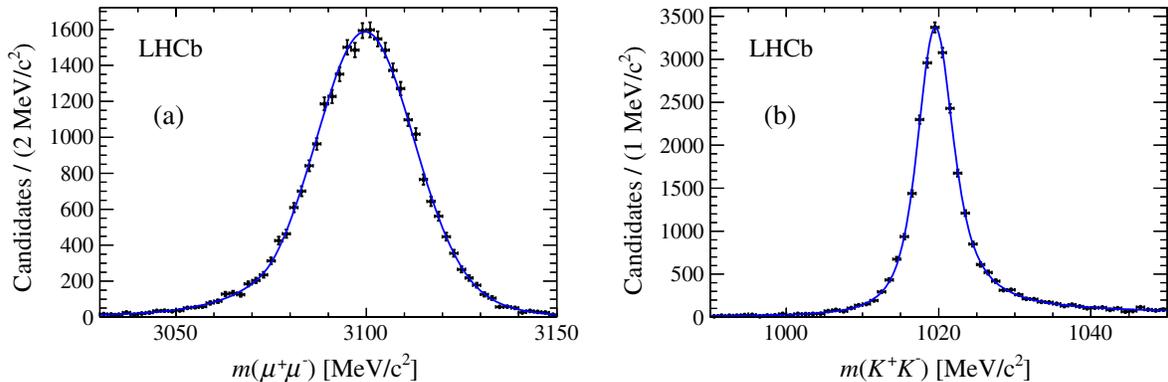

FIG. 5 (color online). Background-subtracted invariant-mass distributions of the (a) $\mu^+ \mu^-$ and (b) $K^+ K^-$ systems in the selected sample of $B_s^0 \rightarrow J/\psi K^+ K^-$ candidates. The solid blue line represents the fit to the data points described in the text.
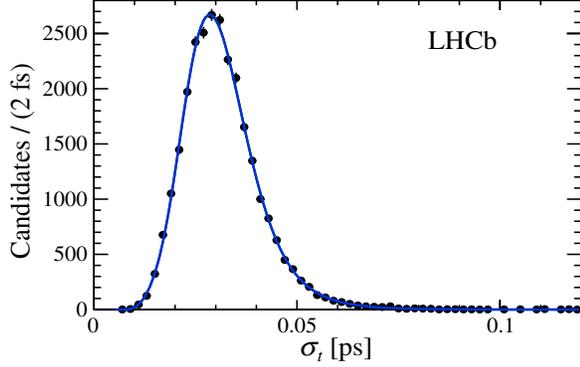
FIG. 6 (color online). Decay-time resolution, σ_t, for selected $B_s^0 \rightarrow J/\psi K^+K^-$ signal events. The curve shows a fit to the data of the sum of two gamma distributions with a common mean.

The resolution model parameters are determined by fitting the distribution with a decay-time model that consists of a prompt peak and two exponential functions, convolved with the resolution model given in Eq. 8.

The per-event resolution receives contributions both from the vertex resolution and from the momentum resolution. The latter contribution is proportional to the decay time and cannot be calibrated with the prompt $J/\psi K^+K^-$ control sample. When using a scale factor for the resolution, there is an assumption that the vertex contribution and the momentum contribution have a common scale. This assumption is tested in simulations, and a systematic uncertainty is assigned.

The effective dilution of the resolution function is calculated by taking its Fourier transform calculated at frequency Δm_s [34]:

$$\mathcal{D} = \int_{-\infty}^{\infty} \mathrm{d}t \cos{(\Delta m_s t)} R(t; \sigma_t). \tag{9}$$

Taking into account the distribution of the per-event resolution, the effective dilution for the calibrated resolution

model is 0.72 ± 0.02. This dilution corresponds to an effective single Gaussian resolution of approximately 45 fs. The systematic uncertainty accounts for uncertainties due to the momentum resolution scale and other differences between the control sample and signal decays. It is derived from simulations.

The sample used to extract the physics parameters of interest consists only of events with $t > 0.3$ ps. The observed decay-time distribution of these events is not sensitive to details of the resolution function. Therefore, in order to simplify the fit procedure, the resolution function for the final fit (described in Sec. VIII) is modelled with a single Gaussian distribution with a resolution scale factor, r_t, chosen such that its effective dilution corresponds to that of the multiple Gaussian model. This scale factor is $r_t = 1.45 \pm 0.06$.

VI. ACCEPTANCE

There are two distinct decay-time acceptance effects that influence the B_s^0 decay-time distribution. First, there is a decrease in reconstruction efficiency for tracks with a large impact parameter with respect to the beam line. This effect is present both in the trigger and the offline reconstruction and translates to a decrease in the B_s^0-meson reconstruction efficiency as a function of its decay time. This decrease is parametrized by a linear acceptance function $\varepsilon_t(t) \propto (1 + \beta t)$, which multiplies the time-dependent $B_s^0 \rightarrow J/\psi K^+K^-$ PDF described below. The parametrization is determined using a control sample of $B^\pm \rightarrow J/\psi K^\pm$ events from data and simulated $B_s^0 \rightarrow J/\psi \phi$ events, leading to $\beta = (-8.3 \pm 4.0) \times 10^{-3}$ ps^{-1}. The uncertainty directly translates to a 4.0×10^{-3} ps^{-1} systematic uncertainty on Γ_s.

Secondly, a nontrivial decay-time acceptance is introduced by the trigger selection. Binned functional descriptions of the acceptance for the unbiased and biased triggers are obtained from the data by exploiting the sample of B_s^0 candidates that

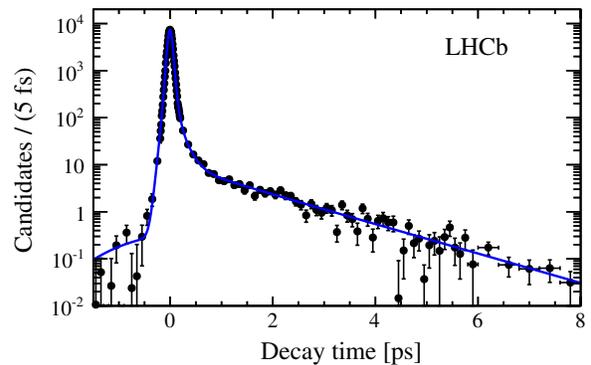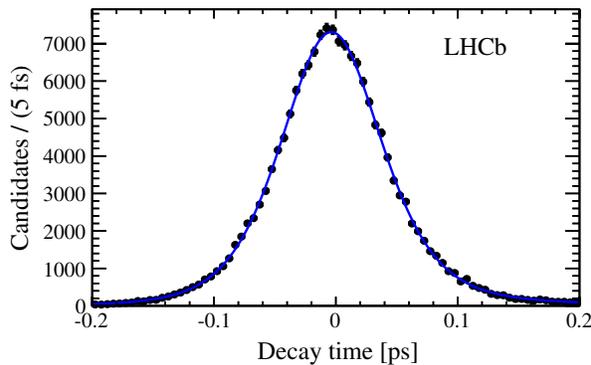

FIG. 7 (color online). Decay-time distribution of prompt $J/\psi K^+K^-$ candidates. The curve (solid blue) is the decay-time model convolved with a Gaussian resolution model. The decay-time model consists of a delta function for the prompt component and two exponential functions with different decay constants, which represent the $B_s^0 \rightarrow J/\psi K^+K^-$ signal and long-lived background, respectively. The decay constants are determined from the fit. The same data set is shown in both plots, on different scales.
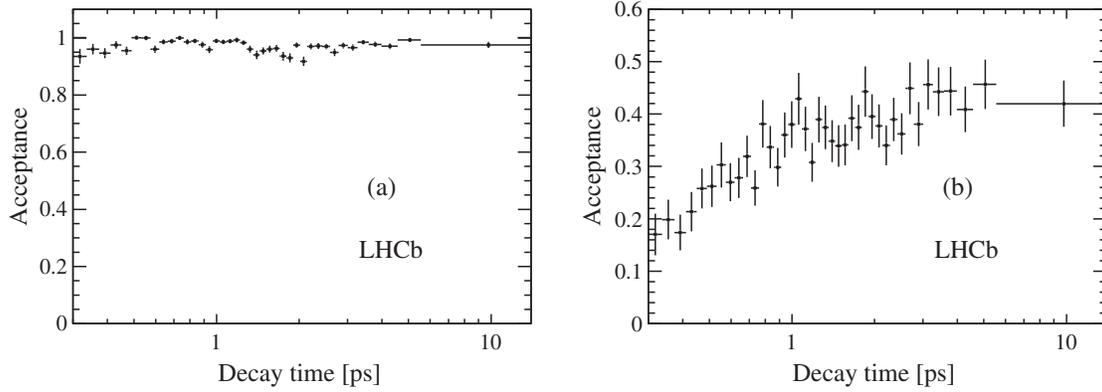
FIG. 8. B_s^0 decay-time trigger-acceptance functions obtained from data. The (a) unbiased trigger category is shown on an absolute scale and the (b) biased trigger category on an arbitrary scale.
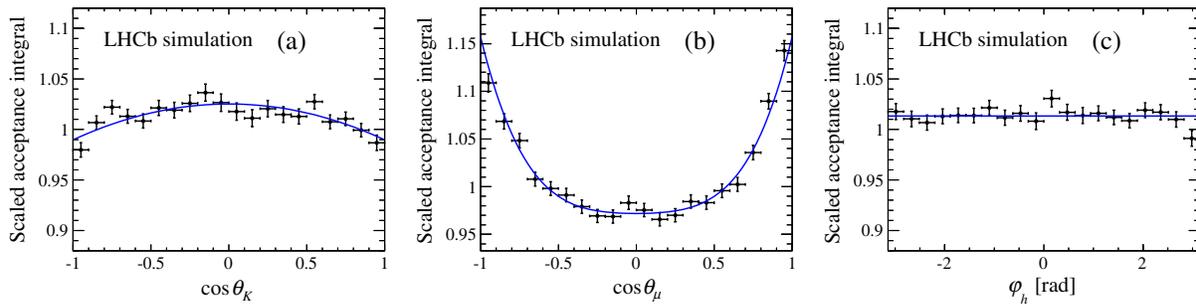

FIG. 9 (color online). Angular acceptance function evaluated with simulated $B_s^0 \rightarrow J/\psi\phi$ events, scaled by the mean acceptance. The acceptance is shown as a function of (a) $\cos\theta_K$, (b) $\cos\theta_\mu$, and (c) φ_h, where in all cases the acceptance is integrated over the other two angles. The points are obtained by summing the inverse values of the underlying physics PDF for simulated events, and the curves represent a polynomial parametrization of the acceptance.

are also selected by a trigger that has no decay-time bias but was only used for a fraction of the recorded data. Figure 8 shows the corresponding acceptance functions that are included in the fit described in Sec. VIII.

The acceptance as a function of the decay angles is not uniform due to the forward geometry of LHCb and the requirements placed upon the momenta of the final-state particles. The three-dimensional acceptance function, ε_Ω, is determined using simulated events that are subjected to the same trigger and selection criteria as the data. Figure 9 shows the angular efficiency as a function of each decay angle, integrated over the other angles. The relative acceptances vary by up to 20% peak to peak. The dominant effect in $\cos\theta_\mu$ is due to the p_T cuts applied to the muons.

The acceptance is included in the unbinned maximum log-likelihood fitting procedure to signal weighted distributions (described in Sec. VIII). Since only a PDF to describe the signal is required, the acceptance function needs to be included only in the normalization of the PDF through the ten integrals $\int d\Omega \varepsilon_\Omega(\Omega) f_k(\Omega)$. The acceptance factors for each event i, $\varepsilon_\Omega(\Omega_i)$, appear only as a constant sum of logarithms and may be ignored in the likelihood maximization. The ten integrals are determined from the fully simulated events using the procedure described in Ref. [35].

VII. TAGGING THE B_s^0 FLAVOR AT PRODUCTION

Each reconstructed candidate is identified by flavor-tagging algorithms as either a B_s^0 meson ($q = +1$) or a $\bar{B}_s^0$ meson ($q = -1$) at production. If the algorithms are unable to make a decision, the candidate is untagged ($q = 0$).

The tagging decision, q, is based upon both opposite-side and same-side tagging algorithms. The opposite-side (OS) tagger relies on the pair production of b and $\bar{b}$ quarks and infers the flavor of the signal B_s^0 meson from the identification of the flavor of the other b hadron. The OS tagger uses the charge of the lepton (μ, e) from semileptonic b decays, the charge of the kaon from the $b \rightarrow c \rightarrow s$ decay chain, and the charge of the inclusive secondary vertex reconstructed from b-hadron decay products. The same-side kaon (SSK) tagger exploits the hadronization process of the $\bar{b}(b)$ quark forming the signal $B_s^0(\bar{B}_s^0)$ meson. In events with a B_s^0 candidate, the fragmentation of a $\bar{b}$ quark can lead to an extra $\bar{s}$ quark being available to form a hadron, often leading to a charged kaon. This kaon is correlated to the signal B_s^0 in phase space, and the sign of the charge identifies its initial flavor.

The probability that the tagging determination is wrong (estimated wrong-tag probability, η) is based upon the output
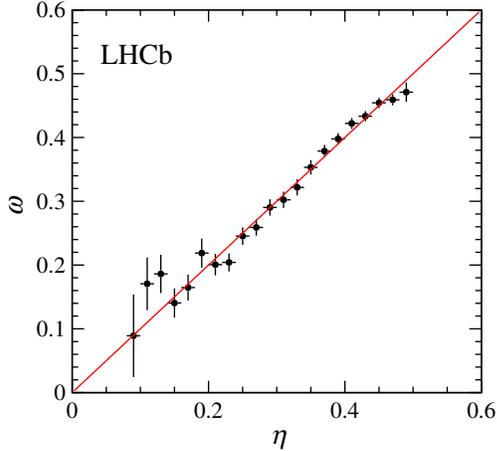
FIG. 10 (color online). Average measured wrong-tag probability (ω) vs estimated wrong-tag probability (η) calibrated on $B^+ \to J/\psi K^+$ signal events for the OS tagging combinations for the background-subtracted events in the signal mass window. Points with errors are data, and the red curve represents the result of the wrong-tag probability calibration, corresponding to the parameters of Table III.

of a neural network trained on simulated events. It is subsequently calibrated with data in order to relate it to the true wrong-tag probability of the event, ω, as described below.

The tagging decision and estimated wrong-tag probability are used event by event in order to maximize the tagging power, $\varepsilon_{\text{tag}} \mathcal{D}^2$, which represents the effective reduction of the signal sample size due to imperfect tagging. In this expression ε_{tag} is the tagging efficiency, i.e., the fraction of events that are assigned a nonzero value of q, and $\mathcal{D} = 1 - 2\omega$ is the dilution.

A. Opposite-side tagging

The OS tagging algorithms and the procedure used to optimize and calibrate them are described in Ref. [36]. In this paper the same approach is used, updated to use the full 2011 data set.

Calibration of the estimated wrong-tag probability, η, is performed using approximately 250,000 $B^+ \to J/\psi K^+$ events selected from data. The values of q and η measured by the OS taggers are compared to the known flavor, which is determined by the charge of the final-state kaon. Figure 10 shows the average wrong-tag probability in the $B^\pm \to J/\psi K^\pm$ control channel in bins of η. For calibration purposes a linear relation is assumed;

$$\omega(\eta) = p_0 + \frac{\Delta p_0}{2} + p_1(\eta - \langle\eta\rangle),$$
$$\bar{\omega}(\eta) = p_0 - \frac{\Delta p_0}{2} + p_1(\eta - \langle\eta\rangle), \quad (10)$$

where $\omega(\eta)$ and $\bar{\omega}(\eta)$ are the calibrated probabilities for a wrong-tag assignment for B and $\bar{B}$ mesons, respectively. This parametrization is chosen to minimize the correlation between the parameters p_0 and p_1. The resulting values of the calibration parameters p_0, p_1, Δp_0, and $\langle\eta\rangle$ (the mean value of η in the sample) are given in Table III. The systematic uncertainties for p_0 and p_1 are determined by comparing the tagging performance for different decay channels, comparing different data-taking periods, and modifying the assumptions of the fit model. The asymmetry parameter Δp_0 is obtained by performing the calibration separately for B^+ and B^- decays. No significant difference of the tagging efficiency or of p_1 is measured ($\Delta\varepsilon_{\text{tag}} = (0.00 \pm 0.10)\%$, $\Delta p_1 = 0.06 \pm 0.04$). Figure 10 shows the relation between ω and η for the full data sample.

The overall effective OS tagging power for $B_s^0 \to J/\psi K^+ K^-$ candidates is $\varepsilon_{\text{tag}} \mathcal{D}^2 = (2.29 \pm 0.06)\%$, with an efficiency of $\varepsilon_{\text{tag}} = (33.00 \pm 0.28)\%$ and an effective average wrong-tag probability of $(36.83 \pm 0.15)\%$ (statistical uncertainties only).

B. Same-side kaon tagging

One of the improvements introduced in this analysis compared to Ref. [5] is the use of the SSK tagger. The SSK tagging algorithm was developed using large samples of simulated B_s^0 decays to $D_s^- \pi^+$ and $J/\psi\phi$ and is documented in Ref. [37]. The algorithm preferentially selects kaons originating from the fragmentation of the signal B_s^0 meson and rejects particles that originate either from the opposite-side B decay or the underlying event. For the optimization, approximately 26,000 $B_s^0 \to D_s^- \pi^+$ data events are used. The same fit procedure employed to determine the B_s^0 mixing frequency Δm_s [38] is used to maximize the effective tagging power $\varepsilon_{\text{tag}} \mathcal{D}^2$.

The calibration was also performed using $B_s^0 \to D_s^- \pi^+$ events and assuming the same linear relation given by Eq. 10. The resulting values of the calibration parameters (p_0, p_1, Δp_0) are given in the second row of Table III. In contrast to the OS tagging case, it is more challenging to measure p_0 and p_1 separately for true B or $\bar{B}$ mesons at production using $B_s^0 \to D_s^- \pi^+$ events. Therefore, assuming that any tagging asymmetry is caused by the difference

TABLE III. Calibration parameters (p_0, p_1, $\langle\eta\rangle$, and Δp_0) corresponding to the OS and SSK taggers. The uncertainties are statistical and systematic, respectively, except for Δp_0 where they have been added in quadrature.

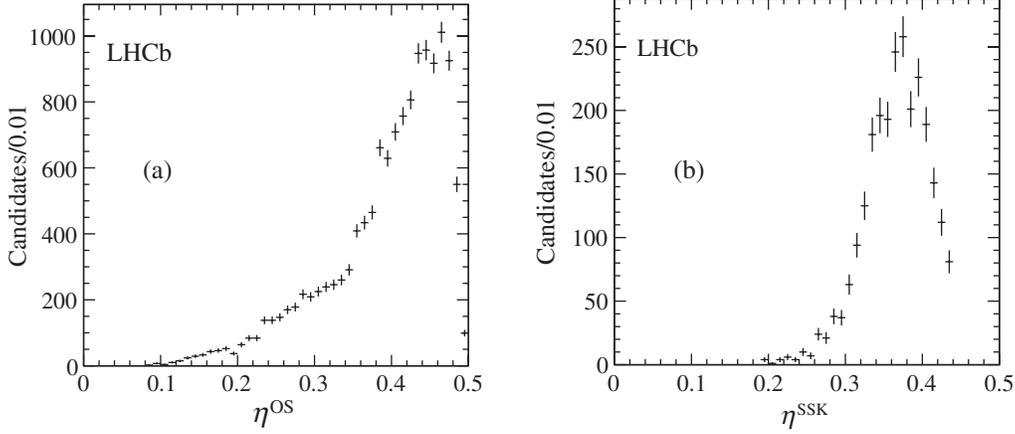| Calibration	p_0	p_1	$\langle\eta\rangle$	Δp_0
OS	$0.392 \pm 0.002 \pm 0.008$	$1.000 \pm 0.020 \pm 0.012$	0.392	0.011 ± 0.003
SSK	$0.350 \pm 0.015 \pm 0.007$	$1.000 \pm 0.160 \pm 0.020$	0.350	-0.019 ± 0.005

FIG. 11.   Distributions of the estimated wrong-tag probability, η, of the $B_s^0 \to J/\psi K^+ K^-$ signal events obtained using the *sPlot* method on the $J/\psi K^+ K^-$ invariant-mass distribution. Both the (a) OS-only and (b) SSK-only tagging categories are shown.

in interaction with matter of K^+ and K^-, Δp_0 is estimated using $B^+ \to J/\psi K^-$, where the p and p_T distributions of the OS tagged kaons are first reweighted to match those of SSK tagged kaons from a large sample of fully simulated $B_s^0 \to D_s^- \pi^+$ events.

The effective SSK tagging power for $B_s^0 \to J/\psi K^+ K^-$ events is $\varepsilon_{tag} \mathcal{D}^2 = (0.89 \pm 0.17)\%$, and the tagging efficiency is $\varepsilon_{tag} = (10.26 \pm 0.18)\%$ (statistical uncertainties only).

C. Combination of OS and SSK tagging

Only a small fraction of tagged events are tagged by both the OS and the SSK algorithms. The algorithms are uncorrelated as they select mutually exclusive charged particles, either in terms of the impact parameter significance with respect to the PV or in terms of the particle identification requirements. The two tagging results are combined taking into account both decisions and their corresponding estimate of η. The combined estimated wrong-tag probability and the corresponding uncertainties are obtained by combining the individual calibrations for the OS and SSK tagging and propagating their uncertainties according to the procedure defined in Ref. [36]. To simplify the fit implementation, the statistical and systematic uncertainties on the combined wrong-tag probability are assumed to be the same for all of these events. They are defined by the average values of the corresponding distributions computed event by event. The effective tagging power for these OS + SSK tagged events is $\varepsilon_{tag} \mathcal{D}^2 = (0.51 \pm 0.03)\%$, and the tagging efficiency is $\varepsilon_{tag} = (3.90 \pm 0.11)\%$.

D. Overall tagging performance

The overall effective tagging power obtained by combining all three categories is $\varepsilon_{tag} \mathcal{D}^2 = (3.13 \pm 0.12 \pm 0.20)\%$, the tagging efficiency is $\varepsilon_{tag} = (39.36 \pm 0.32)\%$, and the wrong-tag probability is $\omega = 35.9\%$. Figure 11 shows the distributions of the estimated wrong-tag

probability η of the $B_s^0 \to J/\psi K^+ K^-$ signal events obtained with the *sPlot* technique using $m(J/\psi K^+ K^-)$ as the discriminating variable.

VIII. MAXIMUM-LIKELIHOOD FIT PROCEDURE

Each event is given a signal weight, W_i, using the *sPlot* [32] method with $m(J/\psi K^+ K^-)$ as the discriminating variable. A weighted fit is then performed using a signal-only PDF, denoted by $\mathcal{S}$, the details of which are described below. The joint negative log likelihood, $\mathcal{L}$, constructed as

$$- \ln \mathcal{L} = -\alpha \sum_{\text{events } i} W_i \ln \mathcal{S}, \qquad (11)$$

is minimized in the fit, where the factor $\alpha = \sum_i W_i / \sum_i W_i^2$ is used to include the effect of the weights in the determination of the uncertainties [39].

A. Mass model used for weighting

The signal mass distribution, $\mathcal{S}_m(m(J/\psi K^+ K^-); m_{B_s^0}, \sigma_m, r_{21}, f_1)$, is modelled by a double Gaussian function. The free parameters in the fit are the common mean, $m_{B_s^0}$; the width of the narrower Gaussian function, σ_m; the ratio of the second to the first Gaussian width, r_{21}; and the fraction of the first Gaussian, f_1.

The background mass distribution, $\mathcal{B}_m(m(J/\psi K^+ K^-))$, is modelled by an exponential function. The full PDF is then constructed as

$$\mathcal{P}_m = f_s \mathcal{S}_m + (1 - f_s) \mathcal{B}_m, \qquad (12)$$

where f_s is the signal fraction. Figure 4 shows the result of fitting this model to the selected candidates.

B. Dividing the data into bins of $m(K^+ K^-)$

The events selected for this analysis are within the $m(K^+ K^-)$ range [990, 1050] MeV/c^2. The data are divided into six independent sets, where the boundaries are given in Table IV. Binning the data this way leads to an improvement

in statistical precision by separating events with different signal fractions, and the analysis becomes insensitive to correction factors, which must be applied to each of the three S-wave interference terms in the differential decay rate (f_8, f_9, f_{10} in Table II). These terms are required to account for an averaging effect resulting from the variation within each bin of the S-wave line shape (assumed to be approximately uniform) relative to that of the P-wave (a relativistic Breit-Wigner function). In each bin, the correction factors are calculated by integrating the product of p with s^*, which appears in the interference terms between the P- and S-wave, where p and s are the normalized $m(K^+K^-)$ line shapes and $*$ is the complex conjugation operator,

$$\int_{m^L}^{m^H} ps^* \mathrm{d}m(K^+K^-) = C_{\mathrm{SP}}e^{-i\theta_{\mathrm{SP}}}, \qquad (13)$$

where $[m^L, m^H]$ denotes the boundaries of the $m(K^+K^-)$ bin, C_{SP} is the correction factor, and θ_{SP} is absorbed in the measurements of $\delta_{\mathrm{S}} - \delta_{\perp}$. The C_{SP} correction factors are given in Table IV. By using several bins, these factors are close to one, whereas if only a single bin were used, the correction would differ substantially from one. The effect of these factors on the fit results is very small and is discussed further in Sec. X, where a different S-wave line shape is considered. Binning the data in $m(K^+K^-)$ allows a repetition of the procedure described in Ref. [40] to resolve the ambiguous solution described in Sec. I by inspecting the trend in the phase difference between the S- and P-wave components.

The weights, W_i, are determined by performing a simultaneous fit to the $m(J/\psi K^+K^-)$ distribution in each of the $m(K^+K^-)$ bins, using a common set of signal mass parameters and six independent background mass parameters. This fit is performed for $m(J/\psi K^+K^-)$ in the range [5200, 5550] MeV/c^2, and the results for the signal mass parameters are shown in Table V.

C. Signal PDF

The physics parameters of interest in this analysis are Γ_s, $\Delta\Gamma_s$, $|A_0|^2$, $|A_\perp|^2$, F_{S}, $\delta_\parallel$, $\delta_\perp$, δ_{S}, ϕ_s, $|\lambda|$ and Δm_s, all of which are defined in Sec. II. The signal PDF, $\mathcal{S}$, is a function of the decay time, t, and angles, Ω, and is

TABLE IV. Bins of $m(K^+K^-)$ used in the analysis and the C_{SP} correction factors for the S-wave interference term, assuming a uniform distribution of nonresonant K^+K^- contribution and a nonrelativistic Breit-Wigner shape for the decays via the ϕ resonance.

$m(K^+K^-)$ bin [MeV/c^2]	C_{SP}
990–1008	0.966
1008–1016	0.956
1016–1020	0.926
1020–1024	0.926
1024–1032	0.956
1032–1050	0.966

conditional upon the estimated wrong-tag probability for the event, η, and the estimate of the decay-time resolution for the event, σ_t. The data are separated into disjoint sets corresponding to each of the possible tagging decisions $q \in \{-1, 0, +1\}$ and the unbiased and biased trigger samples. A separate signal PDF, $\mathcal{S}_q(t, \Omega|\sigma_t, \eta; Z, N)$, is constructed for each event set, where Z represents the physics parameters and N represents nuisance parameters described above.

The $\mathcal{S}_q$ are constructed from the differential decay rates of B_s^0 and $\bar{B}_s^0$ mesons described in Sec. II. Denoting $\frac{\mathrm{d}^4\Gamma(B_s^0 \to J/\psi KK)}{\mathrm{d}t\mathrm{d}\Omega}$ by X and $\frac{\mathrm{d}^4\Gamma(\bar{B}_s^0 \to J/\psi KK)}{\mathrm{d}t\mathrm{d}\Omega}$ by $\bar{X}$, then

$$\mathcal{S}_q = \frac{s_q}{\int s_q \mathrm{d}t\mathrm{d}\Omega}, \qquad (14)$$

where

$$s_{+1} = \Big\{[(1-\omega)X(t, \Omega; Z) + \bar{\omega}\,\bar{X}(t, \Omega; Z)]$$
$$\otimes R(t; \sigma_t)\Big\}\varepsilon_t(t)\varepsilon_\Omega(\Omega),$$

$$s_{-1} = \Big\{[\omega X(t, \Omega; Z) + (1-\bar{\omega})\bar{X}(t, \Omega; Z)]$$
$$\otimes R(t; \sigma_t)\Big\}\varepsilon_t(t)\varepsilon_\Omega(\Omega),$$

$$s_0 = \frac{1}{2}\Big\{[X(t, \Omega; Z) + \bar{X}(t, \Omega; Z)] \otimes R(t; \sigma_t)\Big\}\varepsilon_t(t)\varepsilon_\Omega(\Omega). \qquad (15)$$

Asymmetries in the tagging efficiencies and relative magnitudes of the production rates for B_s^0 and $\bar{B}_s^0$ mesons, as well as the factor $|p/q|^2$, are not included in the model. Sensitivity to these effects is reduced by the use of separately normalized PDFs for each of the tagging decisions, and any residual effect is shown to be negligible.

All physics parameters are free in the fit apart from Δm_s, which is constrained to the value measured by LHCb of 17.63 ± 0.11 ps^{-1} [38]. The parameter $\delta_{\mathrm{S}} - \delta_\perp$ is used in the minimization instead of δ_{S} as there is a large (90%) correlation between δ_{S} and $\delta_\perp$.

In these expressions the terms ω and $\bar{\omega}$ represent the wrong-tag probabilities for a candidate produced as a genuine B_s^0 or $\bar{B}_s^0$ meson, respectively, and are a function of η and the (nuisance) calibration parameters $(p_1, p_0, \langle\eta\rangle, \Delta p_0)$ as given in Eq. 10. The calibration parameters are given in Table III and are all included in

TABLE V. Parameters of the common signal fit to the $m(J/\psi K^+K^-)$ distribution in data.

Parameter	Value
$m_{B_s^0}$ [MeV/c^2]	5368.22 ± 0.05
σ_m [MeV/c^2]	6.08 ± 0.13
f_1	0.760 ± 0.035
r_{21}	2.07 ± 0.09

the fit via Gaussian constraints with widths equal to their uncertainties.

The expressions are convolved with the decay-time resolution function, $R(t; \sigma_t)$ (Sec. V). The scale factor parameter, r_t, is included in the fit with its value constrained by a Gaussian constraint with width equal to its uncertainty. The $\varepsilon_t(t)$ and $\varepsilon_\Omega(\Omega)$ terms are the decay-time acceptance and decay-angle acceptance, respectively. The two different trigger samples have different decay-time acceptance functions. These are described in Sec. VI.

Since this weighted fit uses only a signal PDF, there is no need to include the distributions of either the estimated wrong-tag probability, η, or the decay-time resolution for each event, σ_t. The physics parameter estimation is then performed by a simultaneous fit to the weighted data in each of the $m(K^+K^-)$ bins for each of the two trigger samples. All parameters are common, except for the S-wave fraction F_S and the phase difference $\delta_S - \delta_\perp$, which are independent parameters for each range.

IX. RESULTS FOR $B_s^0 \to J/\psi K^+ K^-$ DECAYS

The results of the fit for the principal physics parameters are given in Table VI for the solution with $\Delta\Gamma_s > 0$, showing both the statistical and the total systematic uncertainties described in Sec. X.

The statistical correlation matrix is shown in Table VII. The projections of the decay-time and angular distributions

TABLE VI. Results of the maximum-likelihood fit for the principal physics parameters. The first uncertainty is statistical, and the second is systematic. The value of Δm_s was constrained to the measurement reported in Ref. [38]. The evaluation of the systematic uncertainties is described in Sec. X.

Parameter	Value
Γ_s [ps^{-1}]	$0.663 \pm 0.005 \pm 0.006$
$\Delta\Gamma_s$ [ps^{-1}]	$0.100 \pm 0.016 \pm 0.003$
$|A_\perp|^2$	$0.249 \pm 0.009 \pm 0.006$
$|A_0|^2$	$0.521 \pm 0.006 \pm 0.010$
$\delta_\parallel$ [rad]	$3.30^{+0.13}_{-0.21} \pm 0.08$
$\delta_\perp$ [rad]	$3.07 \pm 0.22 \pm 0.08$
ϕ_s [rad]	$0.07 \pm 0.09 \pm 0.01$
$|\lambda|$	$0.94 \pm 0.03 \pm 0.02$

are shown in Fig. 12. It was verified that the observed uncertainties are compatible with the expected sensitivities by generating and fitting to a large number of simulated experiments.

Figure 13 shows the 68%, 90%, and 95% C.L. contours obtained from the two-dimensional profile likelihood ratio in the $(\Delta\Gamma_s, \phi_s)$ plane, corresponding to decreases in the log-likelihood of 1.15, 2.30, and 3.00, respectively. Only statistical uncertainties are included. The SM expectation [41] is shown.

The results for the S-wave parameters are shown in Table VIII. The likelihood profiles for these parameters are nonparabolic and are asymmetric. Therefore, the 68% C.L. intervals obtained from the likelihood profiles, corresponding to a decrease of 0.5 in the log-likelihood, are reported. The variation of $\delta_S - \delta_\perp$ with $m(K^+K^-)$ is shown in Fig. 14. The decreasing trend confirms that expected for the physical solution with ϕ_s close to zero, as found in Ref. [40].

All results have been checked by splitting the data set into subsamples to compare different data-taking periods, magnet polarities, B_s^0 tags, and trigger categories. In all cases the results are consistent between the independent subsamples. The measurements of ϕ_s, $\Delta\Gamma_s$, and Γ_s are the most precise to date. Both $\Delta\Gamma_s$ and ϕ_s agree well with the SM expectation [2,41].

These data also allow an independent measurement of Δm_s without constraining it to the value reported in Ref. [38]. This is possible because there are several terms in the differential decay rate of Eq. 1, principally h_4 and h_6, which contain sinusoidal terms in $\Delta m_s t$ that are not multiplied by $\sin\phi_s$. Figure 15 shows the likelihood profile as a function of Δm_s from a fit to the data where Δm_s is not constrained. The result of the fit gives

$$\Delta m_s = 17.70 \pm 0.10(\text{stat}) \pm 0.01(\text{syst}) \text{ ps}^{-1},$$

which is consistent with other measurements [38,42–44].

X. SYSTEMATIC UNCERTAINTIES FOR $B_s^0 \to J/\psi K^+ K^-$ DECAYS

The parameters, Δm_s; the tagging calibration parameters; and the event-by-event proper time scaling factor, r_t, are all allowed to vary within their uncertainties in the fit.

TABLE VII. Correlation matrix for the principal physics parameters.

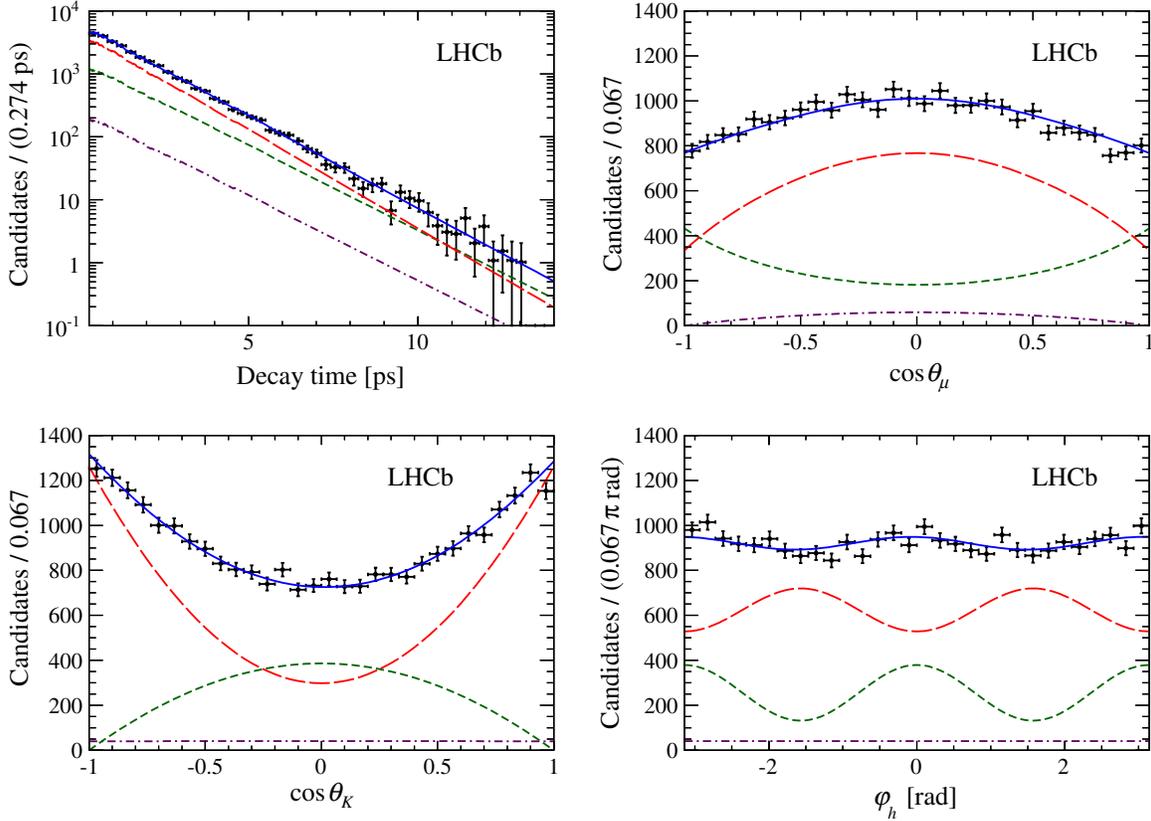|	Γ_s [ps^{-1}]	$\Delta\Gamma_s$ [ps^{-1}]	$|A_\perp|^2$	$|A_0|^2$	$\delta_\parallel$ [rad]	$\delta_\perp$ [rad]	ϕ_s [rad]	$|\lambda|$
Γ_s [ps^{-1}]	1.00	-0.39	0.37	-0.27	-0.09	-0.03	0.06	0.03
$\Delta\Gamma_s$ [ps^{-1}]		1.00	-0.68	0.63	0.03	0.04	-0.04	0.00
$|A_\perp|^2$			1.00	-0.58	-0.28	-0.09	0.08	-0.04
$|A_0|^2$				1.00	-0.02	-0.00	-0.05	0.02
$\delta_\parallel$ [rad]					1.00	0.32	-0.03	0.05
$\delta_\perp$ [rad]						1.00	0.28	0.00
ϕ_s [rad]							1.00	0.04
$|\lambda|$								1.00

FIG. 12 (color online). Decay-time and helicity-angle distributions for $B_s^0 \rightarrow J/\psi K^+ K^-$ decays (data points) with the one-dimensional projections of the PDF at the maximal-likelihood point. The solid blue line shows the total signal contribution, which is composed of *CP*-even (long-dashed red), *CP*-odd (short-dashed green), and S-wave (dotted-dashed purple) contributions.

Therefore, the systematic uncertainties from these sources are included in the statistical uncertainty on the physics parameters. The remaining systematic effects are discussed below and summarized in Tables IX, X, and XI.

The parameters of the $m(J/\psi K^+ K^-)$ fit model are varied within their uncertainties, and a new set of event weights are calculated. Repeating the full decay time and

FIG. 13 (color online). Two-dimensional profile likelihood in the $(\Delta\Gamma_s, \phi_s)$ plane for the $B_s^0 \rightarrow J/\psi K^+ K^-$ data set. Only the statistical uncertainty is included. The SM expectation of $\Delta\Gamma_s = 0.087 \pm 0.021$ ps^{-1} and $\phi_s = -0.036 \pm 0.002$ rad is shown as the black point with error bar [2,41].

angular fit using the new weights gives negligible differences with respect to the results of the nominal fit. The assumption that $m(J/\psi K^+ K^-)$ is independent of the decay-time and angle variables is tested by reevaluating the weights in bins of the decay time and angles. Repeating the full fit with the modified weights gives new estimates of the physics parameter values in each bin. The total systematic uncertainty is computed from the square root of the sum of the individual variances, weighted by the number of signal events in each bin in cases where a significant difference is observed.

Using simulated events, the only identified peaking background is from $B^0 \rightarrow J/\psi K^*(892)^0$ events where the pion from the $K^*(892)^0$ decay is misidentified as a kaon. The fraction of this contribution was estimated from the simulation to be at most 1.5% for $m(J/\psi K^+ K^-)$ in the range [5200, 5550] MeV/c^2. The effect of this background (which is not included in the PDF modelling) was estimated by embedding the simulated $B^0 \rightarrow J/\psi K^*(892)^0$ events in the signal sample and repeating the fit. The resulting variations are taken as systematic uncertainties. The contribution of B_s^0 mesons coming from the decay of B_c^+ mesons is estimated to be negligible.

Since the angular acceptance function, ε_Ω, is determined from simulated events, it is important that the

TABLE VIII. Results of the maximum-likelihood fit for the S-wave parameters, with asymmetric statistical and symmetric systematic uncertainties. The evaluation of the systematic uncertainties is described in Sec. X.

$m(K^+K^-)$ bin [MeV/c^2]	Parameter	Value	σ_{stat} (asymmetric)	σ_{syst}
990–1008	F_S	0.227	+0.081, −0.073	0.020
	$\delta_S - \delta_\perp$ [rad]	1.31	+0.78, −0.49	0.09
1008–1016	F_S	0.067	+0.030, −0.027	0.009
	$\delta_S - \delta_\perp$ [rad]	0.77	+0.38, −0.23	0.08
1016–1020	F_S	0.008	+0.014, −0.007	0.005
	$\delta_S - \delta_\perp$ [rad]	0.51	+1.40, −0.30	0.20
1020–1024	F_S	0.016	+0.012, −0.009	0.006
	$\delta_S - \delta_\perp$ [rad]	−0.51	+0.21, −0.35	0.15
1024–1032	F_S	0.055	+0.027, −0.025	0.008
	$\delta_S - \delta_\perp$ [rad]	−0.46	+0.18, −0.26	0.05
1032–1050	F_S	0.167	+0.043, −0.042	0.021
	$\delta_S - \delta_\perp$ [rad]	−0.65	+0.18, −0.22	0.06

simulation gives a good description of the dependence of final-state particle efficiencies on their kinematic properties. Figure 16 shows significant discrepancies between simulated $B_s^0 \to J/\psi\phi$ events and selected $B_s^0 \to J/\psi K^+K^-$ data events where the background has been subtracted. To account for this difference, the simulated events are reweighted such that the kaon momentum distribution matches the data (reweighting the muon momentum has a negligible effect). A systematic uncertainty is estimated by determining ε_Ω after this reweighting and repeating the fit. The changes observed in physics parameters are taken as systematic uncertainties. A systematic uncertainty is included, which arises from the limited size of the simulated data sample used to determine ε_Ω.

The lower decay-time acceptance is included in the PDF using the binned functions described in Sec. VI. A

systematic uncertainty is determined by repeating the fits with the bin values varied randomly within their statistical precision. The standard deviation of the distribution of central values obtained for each fit parameter is then assigned as the systematic uncertainty. The slope of the acceptance correction at large lifetimes is $\beta = (-8.3 \pm 4.0) \times 10^{-3}$ ps^{-1}. This leads to a 4.0×10^{-3} ps^{-1} systematic uncertainty on Γ_s.

The uncertainty on the LHCb length scale is estimated to be at most 0.020%, which translates directly in an uncertainty on Γ_s and $\Delta\Gamma_s$ of 0.020% with other parameters being unaffected. The momentum scale uncertainty is at most 0.022%. As it affects both the reconstructed momentum and mass of the B_s^0 meson, it cancels to a large extent, and the resulting effect on Γ_s and $\Delta\Gamma_s$ is negligible.

The C_{SP} factors (Table IV) used in the nominal fit assume a nonresonant shape for the S-wave contribution. As a cross-check, the factors are reevaluated assuming a Flatté shape [45], and the fit is repeated. There is a negligible effect on all physics parameters except $\delta_S - \delta_\perp$. A small shift (approximately 10% of the statistical
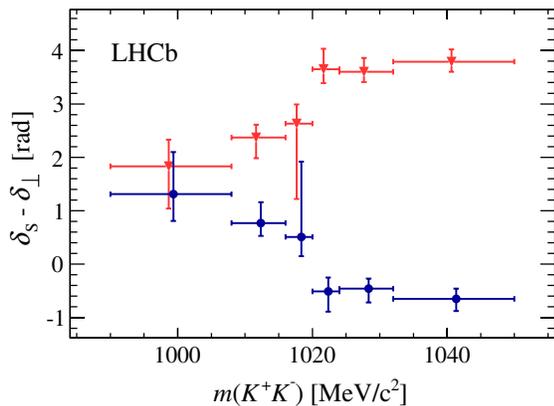

FIG. 14 (color online).   Variation of $\delta_S - \delta_\perp$ with $m(K^+K^-)$, where the uncertainties are the quadrature sum of the statistical and systematic uncertainties in each bin. The decreasing phase trend (blue circles) corresponds to the physical solution with ϕ_s close to zero and $\Delta\Gamma_s > 0$. The ambiguous solution is also shown.
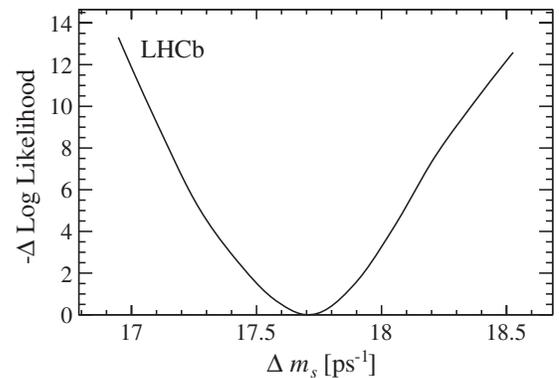

FIG. 15. Profile likelihood for Δm_s from a fit where Δm_s is unconstrained.

TABLE IX.   Statistical and systematic uncertainties.

Source	Γ_s [ps^{-1}]	$\Delta\Gamma_s$ [ps^{-1}]	$|A_\perp|^2$	$|A_0|^2$	$\delta_\parallel$ [rad]	$\delta_\perp$ [rad]	ϕ_s [rad]	$|\lambda|$
Statistical uncertainty	0.0048	0.016	0.0086	0.0061	$^{+0.13}_{-0.21}$	0.22	0.091	0.031
Background subtraction	0.0041	0.002	$\cdots$	0.0031	0.03	0.02	0.003	0.003
$B^0 \to J/\psi K^{*0}$ background	$\cdots$	0.001	0.0030	0.0001	0.01	0.02	0.004	0.005
Angular acceptance reweighting	0.0007	$\cdots$	0.0052	0.0091	0.07	0.05	0.003	0.020
Angular acceptance statistical	0.0002	$\cdots$	0.0020	0.0010	0.03	0.04	0.007	0.006
Lower decay-time acceptance model	0.0023	0.002	$\cdots$	$\cdots$	$\cdots$	$\cdots$	$\cdots$	$\cdots$
Upper decay-time acceptance model	0.0040	$\cdots$	$\cdots$	$\cdots$	$\cdots$	$\cdots$	$\cdots$	$\cdots$
Length and momentum scales	0.0002	$\cdots$	$\cdots$	$\cdots$	$\cdots$	$\cdots$	$\cdots$	$\cdots$
Fit bias	$\cdots$	$\cdots$	0.0010	$\cdots$	$\cdots$	$\cdots$	$\cdots$	$\cdots$
Decay-time resolution offset	$\cdots$	$\cdots$	$\cdots$	$\cdots$	$\cdots$	0.04	0.006	$\cdots$
Quadratic sum of systematics	0.0063	0.003	0.0064	0.0097	0.08	0.08	0.011	0.022
Total uncertainties	0.0079	0.016	0.0107	0.0114	$^{+0.15}_{-0.23}$	0.23	0.092	0.038

TABLE X.   Statistical and systematic uncertainties for S-wave fractions in bins of $m(K^+K^-)$.

Source	Bin 1 F_S	Bin 2 F_S	Bin 3 F_S	Bin 4 F_S	Bin 5 F_S	Bin 6 F_S
Statistical uncertainty	$^{+0.081}_{-0.073}$	$^{+0.030}_{-0.027}$	$^{+0.014}_{-0.007}$	$^{+0.012}_{-0.009}$	$^{+0.027}_{-0.025}$	$^{+0.043}_{-0.042}$
Background subtraction	0.014	0.003	0.001	0.002	0.004	0.006
$B^0 \to J/\psi K^{*0}$ background	0.010	0.006	0.001	0.001	0.002	0.018
Angular acceptance reweighting	0.004	0.006	0.004	0.005	0.006	0.007
Angular acceptance statistical	0.003	0.003	0.002	0.001	0.003	0.004
Fit bias	0.009	$\cdots$	0.002	0.002	0.001	0.001
Quadratic sum of systematics	0.020	0.009	0.005	0.006	0.008	0.021
Total uncertainties	$^{+0.083}_{-0.076}$	$^{+0.031}_{-0.029}$	$^{+0.015}_{-0.009}$	$^{+0.013}_{-0.011}$	$^{+0.028}_{-0.026}$	$^{+0.048}_{-0.047}$

TABLE XI.   Statistical and systematic uncertainties for S-wave phases in bins of $m(K^+K^-)$.

Source	Bin 1 $\delta_S - \delta_\perp$ [rad]	Bin 2 $\delta_S - \delta_\perp$ [rad]	Bin 3 $\delta_S - \delta_\perp$ [rad]	Bin 4 $\delta_S - \delta_\perp$ [rad]	Bin 5 $\delta_S - \delta_\perp$ [rad]	Bin 6 $\delta_S - \delta_\perp$ [rad]
Statistical uncertainty	$^{+0.78}_{-0.49}$	$^{+0.38}_{-0.23}$	$^{+1.40}_{-0.30}$	$^{+0.21}_{-0.35}$	$^{+0.18}_{-0.26}$	$^{+0.18}_{-0.22}$
Background subtraction	0.03	0.02	$\cdots$	0.03	0.01	0.01
$B^0 \to J/\psi K^{*0}$ background	0.08	0.04	0.08	0.01	0.01	0.05
Angular acceptance reweighting	0.02	0.03	0.12	0.13	0.03	0.01
Angular acceptance statistical	0.033	0.023	0.067	0.036	0.019	0.015
Fit bias	0.005	0.043	0.112	0.049	0.022	0.016
C_{SP} factors	0.007	0.028	0.049	0.025	0.021	0.020
Quadratic sum of systematics	0.09	0.08	0.20	0.15	0.05	0.06
Total uncertainties	$^{+0.79}_{-0.50}$	$^{+0.39}_{-0.24}$	$^{+1.41}_{-0.36}$	$^{+0.26}_{-0.38}$	$^{+0.19}_{-0.26}$	$^{+0.19}_{-0.23}$

uncertainty) is observed in $\delta_S - \delta_\perp$ in each bin of $m(K^+K^-)$ and is assigned as a systematic uncertainty.

A possible bias of the fitting procedure is investigated by generating and fitting many simplified simulated experiments of equivalent size to the data sample. The resulting biases are small, and those that are not compatible with zero within three standard deviations are quoted as systematic uncertainties.

The small offset, d, in the decay-time resolution model was set to zero during the fitting procedure. A corresponding systematic uncertainty was evaluated using simulated experiments and found to be negligible for all parameters apart from ϕ_s and $\delta_\perp$.

A measurement of the asymmetry that results from CP violation in the interference between B_s^0-$\bar{B}_s^0$ mixing and decay is potentially affected by CP violation in the mixing, direct CP violation in the decay, production asymmetry, and tagging asymmetry. In the previous analysis [5], an explicit systematic uncertainty was included to account for this. In this analysis the fit parameter $|\lambda|$ is added, separate
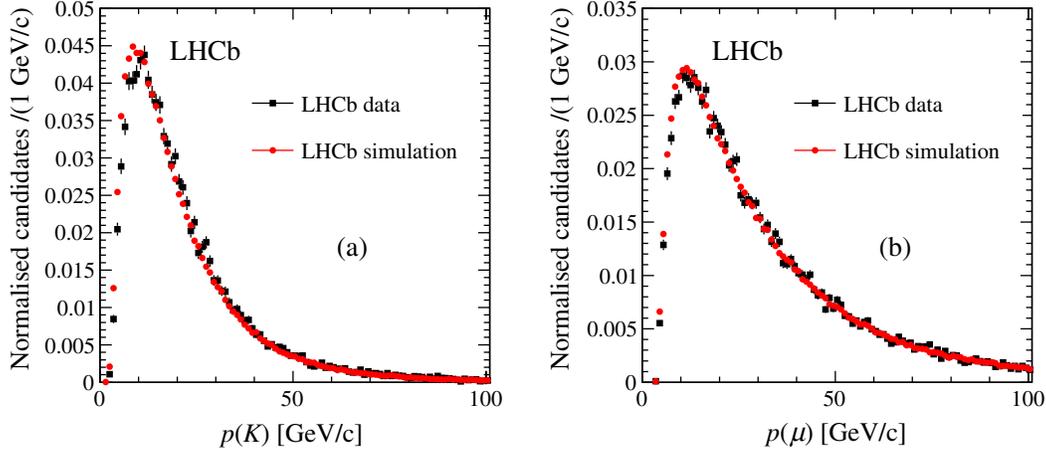
FIG. 16 (color online).   Background-subtracted (a) kaon and (b) muon momentum distributions for $B_s^0 \to J/\psi K^+ K^-$ signal events in data compared to simulated $B_s^0 \to J/\psi \phi$ signal events. The distributions are normalized to the same area. A larger deviation is visible for kaons.

tagging calibrations are used for B_s^0 and $\bar{B}_s^0$ decisions, as well as separate normalizations of the PDF for each tagging decision. Any residual effects due to tagging efficiency asymmetry and production asymmetry are shown to be negligible through simulation studies.

The measurement of Δm_s determined from these data alone without applying a constraint has been reported in Sec. IX. The dominant sources of systematic uncertainty come from the knowledge of the LHCb length and momentum scales. No significant systematic effect is observed after varying the decay-time and angular acceptances and the decay-time resolution. Adding all contributions in quadrature gives a total systematic uncertainty of ± 0.01 ps^{-1}.

XI. RESULTS FOR $B_s^0 \to J/\psi \pi^+ \pi^-$ DECAYS

The $B_s^0 \to J/\psi \pi^+ \pi^-$ analysis used in this paper is unchanged with respect to Ref. [6] except for:

(1) the inclusion of the same-side kaon tagger in the same manner as has already been described for the $B_s^0 \to J/\psi K^+ K^-$ sample. This increases the number of tagged signal candidates to 2146 OS-only, 497 SSK-only, and 293 overlapped events compared to 2445 in Ref. [6]. The overall tagging efficiency is $(39.5 \pm 0.7)\%$, and the tagging power increases from $(2.43 \pm 0.08 \pm 0.26)\%$ to $(3.37 \pm 0.12 \pm 0.27)\%$;

(2) an updated decay-time acceptance model. For this, the decay channel $B^0 \to J/\psi K^*(892)^0$, which has a well-known lifetime, is used to calibrate the decay-time acceptance, and simulated events are used to determine a small relative correction between the acceptances for the $B^0 \to J/\psi K^*(892)^0$ and $B_s^0 \to J/\psi \pi^+ \pi^-$ decays;

(3) the use of the updated values of Γ_s and $\Delta\Gamma_s$ from the $B_s^0 \to J/\psi K^+ K^-$ analysis presented in this paper as constraints in the fit for ϕ_s.

The measurement of ϕ_s using only the $B_s^0 \to J/\psi \pi^+ \pi^-$ events is

$$\phi_s = -0.14^{+0.17}_{-0.16} \pm 0.01 \text{ rad,}$$

where the systematic uncertainty is obtained in the same way as described in Ref. [6]. The decay-time resolution in this channel is approximately 40 fs, and its effect is included in the systematic uncertainty.

In addition, the effective lifetime $\tau_{B_s^0 \to J/\psi \pi^+ \pi^-}^{\text{eff}}$ is measured by fitting a single exponential function to the B_s^0 decay-time distribution with no external constraints on Γ_s and $\Delta\Gamma_s$ applied. The result is

$$\tau_{B_s^0 \to J/\psi \pi^+ \pi^-}^{\text{eff}} = 1.652 \pm 0.024(\text{stat}) \pm 0.024(\text{syst}) \text{ ps.}$$

This is equivalent to a decay width of

$$\Gamma_{B_s^0 \to J/\psi \pi^+ \pi^-}^{\text{eff}} = 0.605 \pm 0.009(\text{stat}) \pm 0.009(\text{syst}) \text{ ps}^{-1},$$

which, in the limit $\phi_s = 0$ and $|\lambda| = 1$, corresponds to Γ_{H}. This result supersedes that reported in Ref. [46]. The uncertainty on the B^0 lifetime [11] used to calibrate the decay-time acceptance is included in the statistical uncertainty. The remaining systematic uncertainty is evaluated by changing the background model and assigning half of the relative change between the fit results with and without the decay-time acceptance correction included, leading to uncertainties of 0.011 ps and 0.021 ps, respectively. The total systematic uncertainty obtained by adding the two contributions in quadrature is 0.024 ps.

XII. COMBINED RESULTS FOR $B_s^0 \to J/\psi K^+ K^-$ AND $B_s^0 \to J/\psi \pi^+ \pi^-$ DATA SETS

This section presents the results from a simultaneous fit to both $B_s^0 \to J/\psi K^+ K^-$ and $B_s^0 \to J/\psi \pi^+ \pi^-$ data sets. The joint log likelihood is minimized with the common parameters being Γ_s, $\Delta\Gamma_s$, ϕ_s, $|\lambda|$, Δm_s, and the tagging

calibration parameters. The combined results are given in Table XII. The correlation matrix for the principal parameters is given in Table XIII.

For all parameters, except Γ_s and $\Delta\Gamma_s$, the same systematic uncertainties as presented for the stand-alone $B_s^0 \to J/\psi K^+ K^-$ analysis are assigned. For Γ_s and $\Delta\Gamma_s$, additional systematic uncertainties of 0.001 ps^{-1} and 0.006 ps^{-1}, respectively, are included, due to the $B_s^0 \to J/\psi \pi^+ \pi^-$ background model and decay-time acceptance variations described above.

XIII. CONCLUSION

A sample of pp collisions at $\sqrt{s} = 7$ TeV, corresponding to an integrated luminosity of 1.0 fb^{-1}, collected with the LHCb detector is used to select $27\,617 \pm 115$ $B_s^0 \to J/\psi K^+ K^-$ events in a ± 30 MeV/c^2 window around the $\phi(1020)$ meson mass [11]. The effective tagging efficiency from the opposite-side (same-side kaon) tagger is $\varepsilon_{\text{eff}} = 2.29 \pm 0.22\%$ ($0.89 \pm 0.18\%$). A combination of data- and simulation-based techniques is used to correct for detector efficiencies. These data have been analyzed in six bins of $m(K^+K^-)$, allowing the resolution of two symmetric solutions, leading to the single most precise measurements of ϕ_s, Γ_s, and $\Delta\Gamma_s$

$$\phi_s = 0.07 \pm 0.09(\text{stat}) \pm 0.01(\text{syst}) \text{ rad},$$

$$\Gamma_s = 0.663 \pm 0.005(\text{stat}) \pm 0.006(\text{syst}) \text{ ps}^{-1},$$

$$\Delta\Gamma_s = 0.100 \pm 0.016(\text{stat}) \pm 0.003(\text{syst}) \text{ ps}^{-1}.$$

TABLE XII. Results of combined fit to the $B_s^0 \to J/\psi K^+ K^-$ and $B_s^0 \to J/\psi \pi^+ \pi^-$ data sets. The first uncertainty is statistical, and the second is systematic.

Parameter	Value
Γ_s [ps^{-1}]	$0.661 \pm 0.004 \pm 0.006$
$\Delta\Gamma_s$ [ps^{-1}]	$0.106 \pm 0.011 \pm 0.007$
$|A_\perp|^2$	$0.246 \pm 0.007 \pm 0.006$
$|A_0|^2$	$0.523 \pm 0.005 \pm 0.010$
$\delta_\parallel$ [rad]	$3.32^{+0.13}_{-0.21} \pm 0.08$
$\delta_\perp$ [rad]	$3.04 \pm 0.20 \pm 0.08$
ϕ_s [rad]	$0.01 \pm 0.07 \pm 0.01$
$|\lambda|$	$0.93 \pm 0.03 \pm 0.02$

The $B_s^0 \to J/\psi K^+ K^-$ events also allow an independent determination of $\Delta m_s = 17.70 \pm 0.10 \pm 0.01$ ps^{-1}.

The time-dependent *CP*-asymmetry measurement using $B_s^0 \to J/\psi \pi^+ \pi^-$ events from Ref. [6] is updated to include same-side kaon tagger information. The result of performing a combined fit using both $B_s^0 \to J/\psi K^+ K^-$ and $B_s^0 \to J/\psi \pi^+ \pi^-$ events gives

$$\phi_s = 0.01 \pm 0.07(\text{stat}) \pm 0.01(\text{syst}) \text{ rad},$$

$$\Gamma_s = 0.661 \pm 0.004(\text{stat}) \pm 0.006(\text{syst}) \text{ ps}^{-1},$$

$$\Delta\Gamma_s = 0.106 \pm 0.011(\text{stat}) \pm 0.007(\text{syst}) \text{ ps}^{-1}.$$

The measurements of ϕ_s, $\Delta\Gamma_s$, and Γ_s are the most precise to date and are in agreement with SM predictions [2,41]. All measurements using $B_s^0 \to J/\psi K^+ K^-$ decays supersede our previous measurements reported in Ref. [5], and all measurements using $B_s^0 \to J/\psi \pi^+ \pi^-$ decays supersede our previous measurements reported in Ref. [6]. The $B_s^0 \to J/\psi \pi^+ \pi^-$ effective lifetime measurement supersedes that reported in Ref. [46]. The combined results reported in Ref. [6] are superseded by those reported here. Since the combined results for Γ_s and $\Delta\Gamma_s$ include all lifetime information from both channels, they should not be used in conjunction with the $B_s^0 \to J/\psi \pi^+ \pi^-$ effective lifetime measurement.

ACKNOWLEDGMENTS

TABLE XIII. Correlation matrix for statistical uncertainties on combined results.

	Γ_s [ps^{-1}]	$\Delta\Gamma_s$ [ps^{-1}]	$|A_\perp|^2$	$|A_0|^2$	$\delta_\parallel$ [rad]	$\delta_\perp$ [rad]	ϕ_s [rad]	$|\lambda|$
Γ_s [ps^{-1}]	1.00	0.10	0.08	0.03	-0.08	-0.04	0.01	0.00
$\Delta\Gamma_s$ [ps^{-1}]		1.00	-0.49	0.47	0.00	0.00	0.00	-0.01
$|A_\perp|^2$			1.00	-0.40	-0.37	-0.14	0.02	-0.05
$|A_0|^2$				1.00	-0.05	-0.03	-0.01	0.01
$\delta_\parallel$ [rad]					1.00	0.39	-0.01	0.13
$\delta_\perp$ [rad]						1.00	0.21	0.03
ϕ_s [rad]							1.00	0.06
$|\lambda|$								1.00

APPENDIX: DEFINITION OF HELICITY DECAY ANGLES

The helicity angles can be defined in terms of the momenta of the decay particles. The momentum of particle a in the center-of-mass system of S is denoted by $\vec{p}_a^S$. With this convention, unit vectors are defined along the helicity axis in the three center-of-mass systems and the two unit normal vectors of the K^+K^- and $\mu^+\mu^-$ decay planes as

$$\hat{e}_z^{KK\mu\mu} = +\frac{\vec{p}_{\mu^+}^{KK\mu\mu} + \vec{p}_{\mu^-}^{KK\mu\mu}}{|\vec{p}_{\mu^+}^{KK\mu\mu} + \vec{p}_{\mu^-}^{KK\mu\mu}|}, \qquad \hat{e}_z^{KK} = -\frac{\vec{p}_{\mu^+}^{KK} + \vec{p}_{\mu^-}^{KK}}{|\vec{p}_{\mu^+}^{KK} + \vec{p}_{\mu^-}^{KK}|},$$

$$\hat{e}_z^{\mu\mu} = -\frac{\vec{p}_{K^+}^{\mu\mu} + \vec{p}_{K^-}^{\mu\mu}}{|\vec{p}_{K^+}^{\mu\mu} + \vec{p}_{K^-}^{\mu\mu}|}, \qquad \hat{n}_{KK} = \frac{\vec{p}_{K^+}^{KK\mu\mu} \times \vec{p}_{K^-}^{KK\mu\mu}}{|\vec{p}_{K^+}^{KK\mu\mu} \times \vec{p}_{K^-}^{KK\mu\mu}|},$$

$$\hat{n}_{\mu\mu} = \frac{\vec{p}_{\mu^+}^{KK\mu\mu} \times \vec{p}_{\mu^-}^{KK\mu\mu}}{|\vec{p}_{\mu^+}^{KK\mu\mu} \times \vec{p}_{\mu^-}^{KK\mu\mu}|}. \tag{A1}$$

The helicity angles are defined in terms of these vectors as

$$\cos\theta_K = \frac{\vec{p}_{K^+}^{KK}}{|\vec{p}_{K^+}^{KK}|} \cdot \hat{e}_z^{KK}, \qquad \cos\theta_\mu = \frac{\vec{p}_{\mu^+}^{\mu\mu}}{|\vec{p}_{\mu^+}^{\mu\mu}|} \cdot \hat{e}_z^{\mu\mu},$$

$$\cos\varphi_h = \hat{n}_{KK} \cdot \hat{n}_{\mu\mu}, \qquad \sin\varphi_h = (\hat{n}_{KK} \times \hat{n}_{\mu\mu}) \cdot \hat{e}_z^{KK\mu\mu}. \tag{A2}$$

[1] M. Kobayashi and T. Maskawa, Prog. Theor. Phys. **49**, 652 (1973); N. Cabibbo, Phys. Rev. Lett. **10**, 531 (1963).
[2] J. Charles *et al.*, Phys. Rev. D **84**, 033005 (2011).
[3] A. J. Buras, Proc. Sci., EPS-HEP2009 (2009) 024.
[4] C.-W. Chiang, A. Datta, M. Duraisamy, D. London, M. Nagashima, and A. Szynkman, J. High Energy Phys. 04 (2010) 031.
[5] R. Aaij *et al.* (LHCb Collaboration), Phys. Rev. Lett. **108**, 101803 (2012).
[6] R. Aaij *et al.* (LHCb Collaboration), Phys. Lett. B **713**, 378 (2012).
[7] G. Aad *et al.* (ATLAS Collaboration), J. High Energy Phys. 12 (2012) 072.
[8] CMS Collaboration, Report No. CMS-PAS-BPH-11-006.
[9] V. M. Abazov *et al.* (D0 Collaboration), Phys. Rev. D **85**, 032006 (2012).
[10] T. Aaltonen *et al.* (CDF Collaboration), Phys. Rev. Lett. **109**, 171802 (2012).
[11] J. Beringer *et al.* (Particle Data Group), Phys. Rev. D **86**, 010001 (2012).
[12] R. Aaij *et al.* (LHCb Collaboration), Phys. Rev. D **87**, 072004 (2013).
[13] A. S. Dighe, I. Dunietz, H. J. Lipkin, and J. L. Rosner, Phys. Lett. B **369**, 144 (1996).
[14] R. Aaij *et al.* (LHCb Collaboration), arXiv:0912.4179.
[15] S. Faller, R. Fleischer, and T. Mannel, Phys. Rev. D **79**, 014005 (2009).
[16] S. Stone and L. Zhang, Phys. Rev. D **79**, 074024 (2009).
[17] I. Dunietz, R. Fleischer, and U. Nierste, Phys. Rev. D **63**, 114015 (2001).
[18] Y. Xie, P. Clarke, G. Cowan, and F. Muheim, J. High Energy Phys. 09 (2009) 074.
[19] Y. Amhis *et al.* (Heavy Flavor Averaging Group), arXiv:1207.1158.
[20] G. C. Branco, L. Lavoura, and J. P. Silva, Int. ser. monogr. phys. **103**, 1 (1999).
[21] R. Aaij *et al.* (LHCb Collaboration), Phys. Rev. D **86**, 052006 (2012).
[22] R. Aaij *et al.* (LHCb Collaboration), JINST **3**, S08005 (2008).
[23] M. Adinolfi *et al.*, Eur. Phys. J. C **73**, 2431 (2013).
[24] R. Aaij *et al.*, JINST **8**, P04022 (2013).
[25] T. Sjöstrand, S. Mrenna, and P. Skands, J. High Energy Phys. 05 (2006) 026.
[26] I. Belyaev *et al.*, in *Nuclear Science Symposium Conference Record (NSS/MIC)* (IEEE, New York, 2010), p. 1155.
[27] D. J. Lange, Nucl. Instrum. Methods Phys. Res., Sect. A **462**, 152 (2001).
[28] P. Golonka and Z. Was, Eur. Phys. J. C **45**, 97 (2006).
[29] J. Allison *et al.* (GEANT4 Collaboration), IEEE Trans. Nucl. Sci. **53**, 270 (2006); S. Agostinelli *et al.* (GEANT4 Collaboration), Nucl. Instrum. Methods Phys. Res., Sect. A **506**, 250 (2003).
[30] M. Clemencic, G. Corti, S. Easo, C. R. Jones, S. Miglioranzi, M. Pappagallo, and P. Robbe, J. Phys. Conf. Ser. **331**, 032023 (2011).
[31] W. D. Hulsbergen, Nucl. Instrum. Methods Phys. Res., Sect. A **552**, 566 (2005).
[32] M. Pivk and F. R. Le Diberder, Nucl. Instrum. Methods Phys. Res., Sect. A **555**, 356 (2005).
[33] T. Skwarnicki, Ph.D. thesis, Institute of Nuclear Physics, 1986; Report No. DESY-F31-86-02.
[34] H. G. Moser and A. Roussarie, Nucl. Instrum. Methods Phys. Res., Sect. A **384**, 491 (1997).
[35] T. du Pree, Ph.D. thesis, VU University, Amsterdam, 2010; Report No. CERN-THESIS-2010-124, 2010.
[36] R. Aaij *et al.* (LHCb Collaboration), Eur. Phys. J. C **72**, 2022 (2012).
[37] R. Aaij *et al.* (LHCb Collaboration), Report No. LHCb-CONF-2012-033.
[38] R. Aaij *et al.* (LHCb Collaboration), Phys. Lett. B **709**, 177 (2012).

[39] Y. Xie, arXiv:0905.0724.

[40] R. Aaij *et al.* (LHCb Collaboration), Phys. Rev. Lett. **108,** 241801 (2012).

[41] A. Lenz and U. Nierste, J. High Energy Phys. 06 (2007) 072; A. Badin, F. Gabbiani, and A. A. Petrov, Phys. Lett. B **653,** 230 (2007); A. Lenz and U. Nierste, arXiv:1102.4274.

[42] V. Abazov *et al.* (D0 Collaboration), Phys. Rev. Lett. **97,** 021802 (2006).

[43] A. Abulencia *et al.* (CDF Collaboration), Phys. Rev. Lett. **97,** 062003 (2006).

[44] R. Aaij *et al.* (LHCb Collaboration), New J. Phys. **15,** 053021 (2013).

[45] S. M. Flatté, Phys. Lett. **63B,** 228 (1976).

[46] R. Aaij *et al.* (LHCb Collaboration), Phys. Rev. Lett. **109,** 152002 (2012).

R. Aaij,[40] C. Abellan Beteta,[35,n] B. Adeva,[36] M. Adinolfi,[45] C. Adrover,[6] A. Affolder,[51] Z. Ajaltouni,[5] J. Albrecht,[9] F. Alessio,[37] M. Alexander,[50] S. Ali,[40] G. Alkhazov,[29] P. Alvarez Cartelle,[36] A. A. Alves, Jr.,[24,37] S. Amato,[2] S. Amerio,[21] Y. Amhis,[7] L. Anderlini,[17,f] J. Anderson,[39] R. Andreassen,[56] R. B. Appleby,[53] O. Aquines Gutierrez,[10] F. Archilli,[18] A. Artamonov,[34] M. Artuso,[57] E. Aslanides,[6] G. Auriemma,[24,m] S. Bachmann,[11] J. J. Back,[47] C. Baesso,[58] V. Balagura,[30] W. Baldini,[16] R. J. Barlow,[53] C. Barschel,[37] S. Barsuk,[7] W. Barter,[46] Th. Bauer,[40] A. Bay,[38] J. Beddow,[50] F. Bedeschi,[22] I. Bediaga,[1] S. Belogurov,[30] K. Belous,[34] I. Belyaev,[30] E. Ben-Haim,[8] M. Benayoun,[8] G. Bencivenni,[18] S. Benson,[49] J. Benton,[45] A. Berezhnoy,[31] R. Bernet,[39] M.-O. Bettler,[46] M. van Beuzekom,[40] A. Bien,[11] S. Bifani,[12] T. Bird,[53] A. Bizzeti,[17,h] P. M. Bjørnstad,[53] T. Blake,[37] F. Blanc,[38] J. Blouw,[11] S. Blusk,[57] V. Bocci,[24] A. Bondar,[33] N. Bondar,[29] W. Bonivento,[15] S. Borghi,[53] A. Borgia,[57] T. J. V. Bowcock,[51] E. Bowen,[39] C. Bozzi,[16] T. Brambach,[9] J. van den Brand,[41] J. Bressieux,[38] D. Brett,[53] M. Britsch,[10] T. Britton,[57] N. H. Brook,[45] H. Brown,[51] I. Burducea,[28] A. Bursche,[39] G. Busetto,[21,q] J. Buytaert,[37] S. Cadeddu,[15] O. Callot,[7] M. Calvi,[20,j] M. Calvo Gomez,[35,n] A. Camboni,[35] P. Campana,[18,37] A. Carbone,[14,c] G. Carboni,[23,k] R. Cardinale,[19,i] A. Cardini,[15] H. Carranza-Mejia,[49] L. Carson,[52] K. Carvalho Akiba,[2] G. Casse,[51] M. Cattaneo,[37] Ch. Cauet,[9] M. Charles,[54] Ph. Charpentier,[37] P. Chen,[3,38] N. Chiapolini,[39] M. Chrzaszcz,[25] K. Ciba,[37] X. Cid Vidal,[37] G. Ciezarek,[52] P. E. L. Clarke,[49] M. Clemencic,[37] H. V. Cliff,[46] J. Closier,[37] C. Coca,[28] V. Coco,[40] J. Cogan,[6] E. Cogneras,[5] P. Collins,[37] A. Comerma-Montells,[35] A. Contu,[15] A. Cook,[45] M. Coombes,[45] S. Coquereau,[8] G. Corti,[37] B. Couturier,[37] G. A. Cowan,[38] D. C. Craik,[47] S. Cunliffe,[52] R. Currie,[49] C. D'Ambrosio,[37] P. David,[8] P. N. Y. David,[40] I. De Bonis,[4] K. De Bruyn,[40] S. De Capua,[53] M. De Cian,[39] J. M. De Miranda,[1] L. De Paula,[2] W. De Silva,[56] P. De Simone,[18] D. Decamp,[4] M. Deckenhoff,[9] L. Del Buono,[8] D. Derkach,[14] O. Deschamps,[5] F. Dettori,[41] A. Di Canto,[11] H. Dijkstra,[37] M. Dogaru,[28] S. Donleavy,[51] F. Dordei,[11] A. Dosil Suárez,[36] D. Dossett,[47] A. Dovbnya,[42] F. Dupertuis,[38] R. Dzhelyadin,[34] A. Dziurda,[25] A. Dzyuba,[29] S. Easo,[48,37] U. Egede,[52] V. Egorychev,[30] S. Eidelman,[33] D. van Eijk,[40] S. Eisenhardt,[49] U. Eitschberger,[9] R. Ekelhof,[9] L. Eklund,[50,37] I. El Rifai,[5] Ch. Elsasser,[39] D. Elsby,[44] A. Falabella,[14,e] C. Färber,[11] G. Fardell,[49] C. Farinelli,[40] S. Farry,[12] V. Fave,[38] D. Ferguson,[49] V. Fernandez Albor,[36] F. Ferreira Rodrigues,[1] M. Ferro-Luzzi,[37] S. Filippov,[32] M. Fiore,[16] C. Fitzpatrick,[37] M. Fontana,[10] F. Fontanelli,[19,i] R. Forty,[37] O. Francisco,[2] M. Frank,[37] C. Frei,[37] M. Frosini,[17,f] S. Furcas,[20] E. Furfaro,[23] A. Gallas Torreira,[36] D. Galli,[14,c] M. Gandelman,[2] P. Gandini,[57] Y. Gao,[3] J. Garofoli,[57] P. Garosi,[53] J. Garra Tico,[46] L. Garrido,[35] C. Gaspar,[37] R. Gauld,[54] E. Gersabeck,[11] M. Gersabeck,[53] T. Gershon,[47,37] Ph. Ghez,[4] V. Gibson,[46] V. V. Gligorov,[37] C. Göbel,[58] D. Golubkov,[30] A. Golutvin,[52,30,37] A. Gomes,[2] H. Gordon,[54] M. Grabalosa Gándara,[5] R. Graciani Diaz,[35] L. A. Granado Cardoso,[37] E. Graugés,[35] G. Graziani,[17] A. Grecu,[28] E. Greening,[54] S. Gregson,[46] O. Grünberg,[59] B. Gui,[57] E. Gushchin,[32] Yu. Guz,[34,37] T. Gys,[37] C. Hadjivasiliou,[57] G. Haefeli,[38] C. Haen,[37] S. C. Haines,[46] S. Hall,[52] T. Hampson,[45] S. Hansmann-Menzemer,[11] N. Harnew,[54] S. T. Harnew,[45] J. Harrison,[53] T. Hartmann,[59] J. He,[37] V. Heijne,[40] K. Hennessy,[51] P. Henrard,[5] J. A. Hernando Morata,[36] E. van Herwijnen,[37] E. Hicks,[51] D. Hill,[54] M. Hoballah,[5] C. Hombach,[53] P. Hopchev,[4] W. Hulsbergen,[40] P. Hunt,[54] T. Huse,[51] N. Hussain,[54] D. Hutchcroft,[51] D. Hynds,[50] V. Iakovenko,[43] M. Idzik,[26] P. Ilten,[12] R. Jacobsson,[37] A. Jaeger,[11] E. Jans,[40] P. Jaton,[38] F. Jing,[3] M. John,[54] D. Johnson,[54] C. R. Jones,[46] B. Jost,[37] M. Kaballo,[9] S. Kandybei,[42] M. Karacson,[37] T. M. Karbach,[37] I. R. Kenyon,[44] U. Kerzel,[37] T. Ketel,[41] A. Keune,[38] B. Khanji,[20] O. Kochebina,[7] I. Komarov,[38] R. F. Koopman,[41] P. Koppenburg,[40] M. Korolev,[31] A. Kozlinskiy,[40] L. Kravchuk,[32] K. Kreplin,[11] M. Kreps,[47] G. Krocker,[11] P. Krokovny,[33] F. Kruse,[9] M. Kucharczyk,[20,25,j] V. Kudryavtsev,[33] T. Kvaratskheliya,[30,37] V. N. La Thi,[38] D. Lacarrere,[37] G. Lafferty,[53] A. Lai,[15] D. Lambert,[49] R. W. Lambert,[41] E. Lanciotti,[37] G. Lanfranchi,[18,37] C. Langenbruch,[37] T. Latham,[47] C. Lazzeroni,[44] R. Le Gac,[6] J. van Leerdam,[40] J.-P. Lees,[4] R. Lefèvre,[5] A. Leflat,[31] J. Lefrançois,[7] S. Leo,[22] O. Leroy,[6] B. Leverington,[11] Y. Li,[3] L. Li Gioi,[5] M. Liles,[51]

R. Lindner,[37] C. Linn,[11] B. Liu,[3] G. Liu,[37] J. von Loeben,[20] S. Lohn,[37] J. H. Lopes,[2] E. Lopez Asamar,[35] N. Lopez-March,[38] H. Lu,[3] D. Lucchesi,[21,q] J. Luisier,[38] H. Luo,[49] F. Machefert,[7] I. V. Machikhiliyan,[4,30] F. Maciuc,[28] O. Maev,[29,37] S. Malde,[54] G. Manca,[15,d] G. Mancinelli,[6] U. Marconi,[14] R. Märki,[38] J. Marks,[11] G. Martellotti,[24] A. Martens,[8] L. Martin,[54] A. Martín Sánchez,[7] M. Martinelli,[40] D. Martinez Santos,[41] D. Martins Tostes,[2] A. Massafferri,[1] R. Matev,[37] Z. Mathe,[37] C. Matteuzzi,[20] E. Maurice,[6] A. Mazurov,[16,32,37,e] J. McCarthy,[44] R. McNulty,[12] A. Mcnab,[53] B. Meadows,[56,54] F. Meier,[9] M. Meissner,[11] M. Merk,[40] D. A. Milanes,[8] M.-N. Minard,[4] J. Molina Rodriguez,[58] S. Monteil,[5] D. Moran,[53] P. Morawski,[25] M. J. Morello,[22,s] R. Mountain,[57] I. Mous,[40] F. Muheim,[49] K. Müller,[39] R. Muresan,[28] B. Muryn,[26] B. Muster,[38] P. Naik,[45] T. Nakada,[38] R. Nandakumar,[48] I. Nasteva,[1] M. Needham,[49] N. Neufeld,[37] A. D. Nguyen,[38] T. D. Nguyen,[38] C. Nguyen-Mau,[38,p] M. Nicol,[7] V. Niess,[5] R. Niet,[9] N. Nikitin,[31] T. Nikodem,[11] A. Nomerotski,[54] A. Novoselov,[34] A. Oblakowska-Mucha,[26] V. Obraztsov,[34] S. Oggero,[40] S. Ogilvy,[50] O. Okhrimenko,[43] R. Oldeman,[15,d] M. Orlandea,[28] J. M. Otalora Goicochea,[2] P. Owen,[52] A. Oyanguren,[35,o] B. K. Pal,[57] A. Palano,[13,b] M. Palutan,[18] J. Panman,[37] A. Papanestis,[48] M. Pappagallo,[50] C. Parkes,[53] C. J. Parkinson,[52] G. Passaleva,[17] G. D. Patel,[51] M. Patel,[52] G. N. Patrick,[48] C. Patrignani,[19,i] C. Pavel-Nicorescu,[28] A. Pazos Alvarez,[36] A. Pellegrino,[40] G. Penso,[24,l] M. Pepe Altarelli,[37] S. Perazzini,[14,c] D. L. Perego,[20,j] E. Perez Trigo,[36] A. Pérez-Calero Yzquierdo,[35] P. Perret,[5] M. Perrin-Terrin,[6] G. Pessina,[20] K. Petridis,[52] A. Petrolini,[19,i] A. Phan,[57] E. Picatoste Olloqui,[35] B. Pietrzyk,[4] T. Pilař,[47] D. Pinci,[24] S. Playfer,[49] M. Plo Casasus,[36] F. Polci,[8] G. Polok,[25] A. Poluektov,[47,33] E. Polycarpo,[2] D. Popov,[10] B. Popovici,[28] C. Potterat,[35] A. Powell,[54] J. Prisciandaro,[38] V. Pugatch,[43] A. Puig Navarro,[38] G. Punzi,[22,r] W. Qian,[4] J. H. Rademacker,[45] B. Rakotomiaramanana,[38] M. S. Rangel,[2] I. Raniuk,[42] N. Rauschmayr,[37] G. Raven,[41] S. Redford,[54] M. M. Reid,[47] A. C. dos Reis,[1] S. Ricciardi,[48] A. Richards,[52] K. Rinnert,[51] V. Rives Molina,[35] D. A. Roa Romero,[5] P. Robbe,[7] E. Rodrigues,[53] P. Rodriguez Perez,[36] S. Roiser,[37] V. Romanovsky,[34] A. Romero Vidal,[36] J. Rouvinet,[38] T. Ruf,[37] F. Ruffini,[22] H. Ruiz,[35] P. Ruiz Valls,[35,o] G. Sabatino,[24,k] J. J. Saborido Silva,[36] N. Sagidova,[29] P. Sail,[50] B. Saitta,[15,d] C. Salzmann,[39] B. Sanmartin Sedes,[36] M. Sannino,[19,i] R. Santacesaria,[24] C. Santamarina Rios,[36] E. Santovetti,[23,k] M. Sapunov,[6] A. Sarti,[18,l] C. Satriano,[24,m] A. Satta,[23] M. Savrie,[16,e] D. Savrina,[30,31] P. Schaack,[52] M. Schiller,[41] H. Schindler,[37] M. Schlupp,[9] M. Schmelling,[10] B. Schmidt,[37] O. Schneider,[38] A. Schopper,[37] M.-H. Schune,[7] R. Schwemmer,[37] B. Sciascia,[18] A. Sciubba,[24] M. Seco,[36] A. Semennikov,[30] K. Senderowska,[26] I. Sepp,[52] N. Serra,[39] J. Serrano,[6] P. Seyfert,[11] M. Shapkin,[34] I. Shapoval,[16,42] P. Shatalov,[30] Y. Shcheglov,[29] T. Shears,[51,37] L. Shekhtman,[33] O. Shevchenko,[42] V. Shevchenko,[30] A. Shires,[52] R. Silva Coutinho,[47] T. Skwarnicki,[57] N. A. Smith,[51] E. Smith,[54,48] M. Smith,[53] M. D. Sokoloff,[56] F. J. P. Soler,[50] F. Soomro,[18] D. Souza,[45] B. Souza De Paula,[2] B. Spaan,[9] A. Sparkes,[49] P. Spradlin,[50] F. Stagni,[37] S. Stahl,[11] O. Steinkamp,[39] S. Stoica,[28] S. Stone,[57] B. Storaci,[39] M. Straticiuc,[28] U. Straumann,[39] V. K. Subbiah,[37] S. Swientek,[9] V. Syropoulos,[41] M. Szczekowski,[27] P. Szczypka,[38,37] T. Szumlak,[26] S. T'Jampens,[4] M. Teklishyn,[7] E. Teodorescu,[28] F. Teubert,[37] C. Thomas,[54] E. Thomas,[37] J. van Tilburg,[11] V. Tisserand,[4] M. Tobin,[38] S. Tolk,[41] D. Tonelli,[37] S. Topp-Joergensen,[54] N. Torr,[54] E. Tournefier,[4,52] S. Tourneur,[38] M. T. Tran,[38] M. Tresch,[39] A. Tsaregorodtsev,[6] P. Tsopelas,[40] N. Tuning,[40] M. Ubeda Garcia,[37] A. Ukleja,[27] D. Urner,[53] U. Uwer,[11] V. Vagnoni,[14] G. Valenti,[14] R. Vazquez Gomez,[35] P. Vazquez Regueiro,[36] S. Vecchi,[16] J. J. Velthuis,[45] M. Veltri,[17,g] G. Veneziano,[38] M. Vesterinen,[37] B. Viaud,[7] D. Vieira,[2] X. Vilasis-Cardona,[35,n] A. Vollhardt,[39] D. Volyanskyy,[10] D. Voong,[45] A. Vorobyev,[29] V. Vorobyev,[33] C. Voß,[59] H. Voss,[10] R. Waldi,[59] R. Wallace,[12] S. Wandernoth,[11] J. Wang,[57] D. R. Ward,[46] N. K. Watson,[44] A. D. Webber,[53] D. Websdale,[52] M. Whitehead,[47] J. Wicht,[37] J. Wiechczynski,[25] D. Wiedner,[11] L. Wiggers,[40] G. Wilkinson,[54] M. P. Williams,[47,48] M. Williams,[55] F. F. Wilson,[48] J. Wishahi,[9] M. Witek,[25] S. A. Wotton,[46] S. Wright,[46] S. Wu,[3] K. Wyllie,[37] Y. Xie,[49,37] F. Xing,[54] Z. Xing,[57] Z. Yang,[3] R. Young,[49] X. Yuan,[3] O. Yushchenko,[34] M. Zangoli,[14] M. Zavertyaev,[10,a] F. Zhang,[3] L. Zhang,[57] W.C. Zhang,[12] Y. Zhang,[3] A. Zhelezov,[11] A. Zhokhov,[30] L. Zhong,[3] and A. Zvyagin[37]

(LHCb Collaboration)

[1]*Centro Brasileiro de Pesquisas Físicas (CBPF), Rio de Janeiro, Brazil*
[2]*Universidade Federal do Rio de Janeiro (UFRJ), Rio de Janeiro, Brazil*
[3]*Center for High Energy Physics, Tsinghua University, Beijing, China*
[4]*LAPP, Université de Savoie, CNRS/IN2P3, Annecy-Le-Vieux, France*
[5]*Clermont Université, Université Blaise Pascal, CNRS/IN2P3, LPC, Clermont-Ferrand, France*

[6]*CPPM, Aix-Marseille Université, CNRS/IN2P3, Marseille, France*
[7]*LAL, Université Paris-Sud, CNRS/IN2P3, Orsay, France*
[8]*LPNHE, Université Pierre et Marie Curie, Université Paris Diderot, CNRS/IN2P3, Paris, France*
[9]*Fakultät Physik, Technische Universität Dortmund, Dortmund, Germany*
[10]*Max-Planck-Institut für Kernphysik (MPIK), Heidelberg, Germany*
[11]*Physikalisches Institut, Ruprecht-Karls-Universität Heidelberg, Heidelberg, Germany*
[12]*School of Physics, University College Dublin, Dublin, Ireland*
[13]*Sezione INFN di Bari, Bari, Italy*
[14]*Sezione INFN di Bologna, Bologna, Italy*
[15]*Sezione INFN di Cagliari, Cagliari, Italy*
[16]*Sezione INFN di Ferrara, Ferrara, Italy*
[17]*Sezione INFN di Firenze, Firenze, Italy*
[18]*Laboratori Nazionali dell'INFN di Frascati, Frascati, Italy*
[19]*Sezione INFN di Genova, Genova, Italy*
[20]*Sezione INFN di Milano Bicocca, Milano, Italy*
[21]*Sezione INFN di Padova, Padova, Italy*
[22]*Sezione INFN di Pisa, Pisa, Italy*
[23]*Sezione INFN di Roma Tor Vergata, Roma, Italy*
[24]*Sezione INFN di Roma La Sapienza, Roma, Italy*
[25]*Henryk Niewodniczanski Institute of Nuclear Physics Polish Academy of Sciences, Kraków, Poland*
[26]*Faculty of Physics and Applied Computer Science, AGH—University of Science and Technology, Kraków, Poland*
[27]*National Center for Nuclear Research (NCBJ), Warsaw, Poland*
[28]*Horia Hulubei National Institute of Physics and Nuclear Engineering, Bucharest, Magurele, Romania*
[29]*Petersburg Nuclear Physics Institute (PNPI), Gatchina, Russia*
[30]*Institute of Theoretical and Experimental Physics (ITEP), Moscow, Russia*
[31]*Institute of Nuclear Physics, Moscow State University (SINP MSU), Moscow, Russia*
[32]*Institute for Nuclear Research of the Russian Academy of Sciences (INR RAN), Moscow, Russia*
[33]*Budker Institute of Nuclear Physics (SB RAS) and Novosibirsk State University, Novosibirsk, Russia*
[34]*Institute for High Energy Physics (IHEP), Protvino, Russia*
[35]*Universitat de Barcelona, Barcelona, Spain*
[36]*Universidad de Santiago de Compostela, Santiago de Compostela, Spain*
[37]*European Organization for Nuclear Research (CERN), Geneva, Switzerland*
[38]*Ecole Polytechnique Fédérale de Lausanne (EPFL), Lausanne, Switzerland*
[39]*Physik-Institut, Universität Zürich, Zürich, Switzerland*
[40]*Nikhef National Institute for Subatomic Physics, Amsterdam, The Netherlands*
[41]*Nikhef National Institute for Subatomic Physics and VU University Amsterdam, Amsterdam, The Netherlands*
[42]*NSC Kharkiv Institute of Physics and Technology (NSC KIPT), Kharkiv, Ukraine*
[43]*Institute for Nuclear Research of the National Academy of Sciences (KINR), Kyiv, Ukraine*
[44]*University of Birmingham, Birmingham, United Kingdom*
[45]*H.H. Wills Physics Laboratory, University of Bristol, Bristol, United Kingdom*
[46]*Cavendish Laboratory, University of Cambridge, Cambridge, United Kingdom*
[47]*Department of Physics, University of Warwick, Coventry, United Kingdom*
[48]*STFC Rutherford Appleton Laboratory, Didcot, United Kingdom*
[49]*School of Physics and Astronomy, University of Edinburgh, Edinburgh, United Kingdom*
[50]*School of Physics and Astronomy, University of Glasgow, Glasgow, United Kingdom*
[51]*Oliver Lodge Laboratory, University of Liverpool, Liverpool, United Kingdom*
[52]*Imperial College London, London, United Kingdom*
[53]*School of Physics and Astronomy, University of Manchester, Manchester, United Kingdom*
[54]*Department of Physics, University of Oxford, Oxford, United Kingdom*
[55]*Massachusetts Institute of Technology, Cambridge, Massachusetts, USA*
[56]*University of Cincinnati, Cincinnati, Ohio, USA*
[57]*Syracuse University, Syracuse, New York, USA*
[58]*Pontifícia Universidade Católica do Rio de Janeiro (PUC-Rio), Rio de Janeiro, Brazil*
[associated with Universidade Federal do Rio de Janeiro (UFRJ), Rio de Janeiro, Brazil]
[59]*Institut für Physik, Universität Rostock, Rostock, Germany (associated with Physikalisches Institut,*
Ruprecht-Karls-Universität Heidelberg, Heidelberg, Germany)

[a]Also at P.N. Lebedev Physical Institute, Russian Academy of Science (LPI RAS), Moscow, Russia.
[b]Also at Università di Bari, Bari, Italy.
[c]Also at Università di Bologna, Bologna, Italy.

[d]Also at Università di Cagliari, Cagliari, Italy.

[e]Also at Università di Ferrara, Ferrara, Italy.

[f]Also at Università di Firenze, Firenze, Italy.

[g]Also at Università di Urbino, Urbino, Italy.

[h]Also at Università di Modena e Reggio Emilia, Modena, Italy.

[i]Also at Università di Genova, Genova, Italy.

[j]Also at Università di Milano Bicocca, Milano, Italy.

[k]Also at Università di Roma Tor Vergata, Roma, Italy.

[l]Also at Università di Roma La Sapienza, Roma, Italy.

[m]Also at Università della Basilicata, Potenza, Italy.

[n]Also at LIFAELS, La Salle, Universitat Ramon Llull, Barcelona, Spain.

[o]Also at IFIC, Universitat de Valencia-CSIC, Valencia, Spain.

[p]Also at Hanoi University of Science, Hanoi, Vietnam.

[q]Also at Università di Padova, Padova, Italy.

[r]Also at Università di Pisa, Pisa, Italy.

[s]Also at Scuola Normale Superiore, Pisa, Italy.